Hydrodynamic performance of BCF swimmers in high Reynolds numbers with biomimetic applications in Autonomous Underwater Vehicles

National Technical University of Athens
School of Naval Architect and Marine Engineer
Division of Marine Hydrodynamics

Student: Antoniadis Konstantinos
Supervisor: Georgios Papadakis, Assistant Professor
September 2024, Athens

Acknowledgements

This thesis would not have been possible without the guidance, support, and encouragement of numerous individuals, to whom I am deeply grateful.

First and foremost, I would like to express my sincerest gratitude to my supervisor, George Papadakis, and his PhD candidate, Spyridon Zafeiris, for their continuous support, patience, and invaluable guidance throughout the entire research process. This thesis wouldn't have been completed without their help and for that i am grateful.

On a personal note, I would like to express my deepest gratitude to my family for their constant love, patience, and encouragement throughout the ups and downs of this journey. Finally, I am incredibly grateful to my friends, Achilles and Stavroula, and my girlfriend, Konstantina, for their unwavering support in both big and small ways.

To all of you, I offer my sincere thanks.

This page is intentionally left blank.

Contents

Abstract **2**

Acknowledgements **2**

1 Introduction **9**
1.1 The origins of fish locomotion studies. 9
1.2 Modes of Swimming 11
1.2.1 Body and/or Caudal Fin Propulsion 11
1.2.2 Median or Pectoral Fins 15
1.3 What is CFD 15
1.4 Applications of Biomimetics 17

2 Methodology **24**
2.1 Governing Equations 24
2.2 Artificial Compressibility 26
2.3 Definition of a Control Volume 26
2.4 Finite Volume Method 27
2.4.1 Spacial Discretization 28
2.4.2 Temporal Discretization 29
2.5 Grid Deformation 30
2.5.1 Radial Basis Functions (RBF) 31
2.6 Turbulence 32
2.6.1 Turbulence Modelling 33
2.6.2 Menter's k-omega SST model 34

3 Results **37**
3.1 Problem formulation 37
3.2 Grid Independence 39
3.3 Temporal Independence 40
3.4 Thrust dependence on Re, St and λ 40
3.5 Comparison between Laminar and Turbulent Flow 51

4 Conclusions **54**
4.1 Summary 54
4.2 Future Work 54

List of Figures

1.1 Swimming modes associated with (a) BCF propulsion and (b) MPF propulsion. Shaded areas contribute to thrust generation, from [13]. . 11
1.2 BCF swimming modes: (a) anguilliform, (b) subcarangiform, (c) carangiform and (d) thunniform mode. 14
1.3 **(a)** NACA0015 foil, from [18]. **(b)** NACA0012 fish-like foil ,from [16] 18
1.4 A 3D ray model, from [26] 18
1.5 The postures of the three propulsion modes during the movement of the dolphin. (a) Single-stage propulsion, (b) Double-stage propulsion, (c) Multi-stage propulsion, from [33] 19
1.6 Biomimetic ducted propeller geometry, from [44] 21
1.7 (a) Basic propeller, (b) Tubercle propeller, from [44] 21
1.8 Three-dimensional hydrofoil partially covered with micro-grooves: (a) overall model and (b) details of the microgrooves, from [47] 22

2.1 A 2-D control volume. 27
2.2 Reconstruction of variables on the faces. 29

3.1 Computational mesh. 37
3.2 Foil's parameters. 37
3.3 Travelling wavy motion. 37
3.4 Zoomed-in views of the computational grid. 39
3.5 Mesh independence test at $(St, Re, \lambda) = (0.6, 50000, 1.0)$. N_2 is adopted due to its insignificant difference from N_3 and its efficiency. 39
3.6 Time independence test at $(St, Re, \lambda) = (0.6, 50000, 1.0)$. Δ_2 is adopted due to its insignificant difference from Δ_3 and its efficiency. 40
3.7 (a-e) Time-mean thrust coefficient $\overline{C}_T$ as a function of Strouhal number St and wave length λ, denoted as $\overline{C}_T = c_1 St^3 \lambda + c_2$. The dash line is the linear least-squares regression line. (f) Relationship of $\overline{C}_T$ with St, Re and λ for the travelling wavy foil. The dash line denotes a linear function with coefficient equal to one. 42
3.8 (a),(b) Dependence of c_1 and c_2 on Re. The dash lines denote a linear function with coefficient equal to one. 42
3.9 (a)-(e) Thrust coefficient oscillation during one period for $(St, Re) = [(0.2, 10000), (0.4, 25000), (0.6, 50000), (0.8, 100000), (1.0, 200000)]$ respectively. It's obvious that by increasing St and Re, $\overline{C}_T$ is also increased. Increasing λ, $\overline{C}_T$ oscillation amplitude is larger. 43

3.10 Contours of spanwise vorticity for $\lambda = 0.5$. The red and blue colors denote positive and negative vorticity respectively. (a) $(St, Re) = (0.2, 10000)$, (b) $(St, Re) = (0.4, 25000)$, (c) $(St, Re) = (0.6, 50000)$, (d) $(St, Re) = (0.8, 100000)$, (e) $(St, Re) = (1.0, 200000)$ 44
3.11 Contours of spanwise vorticity for $\lambda = 0.67$. (a) $(St, Re) = (0.2, 10000)$, (b) $(St, Re) = (0.4, 25000)$, (c) $(St, Re) = (0.6, 50000)$, (d) $(St, Re) = (0.8, 100000)$, (e) $(St, Re) = (1.0, 200000)$ 45
3.12 Contours of spanwise vorticity for $\lambda = 1.0$. (a) $(St, Re) = (0.2, 10000)$, (b) $(St, Re) = (0.4, 25000)$, (c) $(St, Re) = (0.6, 50000)$, (d) $(St, Re) = (0.8, 100000)$, (e) $(St, Re) = (1.0, 200000)$ 46
3.13 Contours of spanwise vorticity for $\lambda = 1.5$. (a) $(St, Re) = (0.2, 10000)$, (b) $(St, Re) = (0.4, 25000)$, (c) $(St, Re) = (0.6, 50000)$, (d) $(St, Re) = (0.8, 100000)$, (e) $(St, Re) = (1.0, 200000)$ 47
3.14 Contours of spanwise vorticity for $\lambda = 2.0$. (a) $(St, Re) = (0.2, 10000)$, (b) $(St, Re) = (0.4, 25000)$, (c) $(St, Re) = (0.6, 50000)$, (d) $(St, Re) = (0.8, 100000)$, (e) $(St, Re) = (1.0, 200000)$ 48
3.15 Effect of Re on $\overline{C}_T$. Increasing St and λ we get higher values of $\overline{C}_T$. Re doesn't contribute as much as St and λ 49
3.16 Effect of St on $\overline{C}_T$. There is an exponential growth of $\overline{C}_T$ when increasing St and λ at the same time. It's observed that with higher values of Re, $\overline{C}_T$ is minimally affected. 50
3.17 Time-mean thrust coefficient $\overline{C}_T$ as a function of Strouhal number St and wave length λ, denoted as $\overline{C}_T = St^3\lambda$ for small Re, from [57]. . . 51
3.18 (a) Dependence of c_1 and c_2 on Re. (b) Relationship of $\overline{C}_T$ with St, Re and λ for the travelling wavy foil for small Re, from [57]. 52
3.19 Thrust coefficient oscillation during one period for low Reynolds, from [57]. 52

This page is intentionally left blank.

Abstract

Biomimetics, inspired by nature, has become a crucial tool in the development of Autonomous Underwater Vehicles (AUVs). When combined with computational fluid dynamics (CFD), this approach has significantly advanced research in the field by simulating a fish swimming using a NACA 0012 foil. Previous studies have shown the relation of thrust coefficient with St, Re and λ for low Re numbers. Doing so, only the case of laminar flow is examined. In this thesis, simulations are run, using an Eulerian solver (MaPFlow), for higher Re to examine the case of turbulent flow and to make comparisons between the two cases. An unstructured grid was made for these simulations with 1.1×10^5 cells. The time step was chosen at 1.5432×10^{-4} and the values of St, Re and λ at $0.2 - 1.0$, $10000 - 200000$ and $0.5 - 2.0$ respectively. Similar to laminar flow, it's found that for larger Re numbers there is linear relation between $\overline{C}_T$ and $St^3\lambda$. On the other hand, it's found that increasing Re, $\overline{C}_T$ is minimally affected by these increases.

Chapter 1

Introduction

Biomimetics, the practice of drawing inspiration from nature to solve engineering challenges, has become increasingly significant in the design and development of underwater robots. Specifically, the study of fish locomotion offers valuable insights into creating more efficient and adaptable underwater vehicles. Traditional underwater robots, also known as remotely operated robots (ROVs) [1, 2], often propelled by rigid propellers, face multiple challenges in complex marine environments, such as high energy consumption, environmental damage, and limited manoeuvrability [3]. To overcome these limitations, researchers have turned to biomimicry, inspired by the natural swimming mechanisms of fish and other aquatic animals.

Fish, through millions of years of evolution, have perfected the art of movement in water, utilizing their tail and pectoral fins to achieve high manoeuvrability, stability, and efficiency. This has led to the development of biomimetic underwater robots, also know as Autonomous Underwater Vehicle (AUVs), that mimic these natural propulsion methods, offering superior performance in underwater exploration and tasks. These robots, which include designs like the groundbreaking RoboTuna [4], are increasingly favored for their ability to navigate complex environments with agility and precision.

This introduction reviews the principles of fish locomotion, explores the advancements in biomimetic propulsion systems, and highlights their applications in the creation of underwater robots that embody the core concepts of biomimetics.

1.1 The origins of fish locomotion studies.

Understanding the complexities of fish locomotion represents a chronic challenge, with only a fraction of its complexity perceptible to the naked eye. While observing fish in their natural habitat reveals some clues, the underlying mechanisms driving their movements remain largely enigmatic. Current established view suggests that fish locomotion primarily relies on the propagation of alternating waves of muscular contraction along the body. This wave-like motion generates thrust against the surrounding water, facilitating forward movement. However, the specifics of how this propulsion is achieved vary among different fish species.

In many fish, thrust is generated by the oblique backward push of the body

against the water, a motion akin to that of a swimming eel. Alternatively, some fast-swimming species, such as tuna, have evolved to concentrate propulsion efforts in their tail fins, allowing for greater speed and agility. Surprisingly, the paired fins, often thought to play a significant role in forward propulsion, appear to contribute little to conventional swimming and are primarily utilized for manoeuvring and stability. These observations, while challenging to discern through direct observation, underscore the complexity of fish locomotion and its divergence from the terrestrial locomotive habits that humans are more familiar with.

Ancient scholars, such as Aristotle in the fourth century B.C., made early attempts to understand fish locomotion. Aristotle recognized the undulating motion of certain fish species and liken their aquatic movement to the terrestrial locomotion of serpents. However, his understanding was limited, as he mistakenly attributed the primary propulsion to the fins rather than the body and tail. Similarly, the ancient Hindu medical text Susruta-samhita offered insights into the correlation between fish body shape, habitat, and locomotion patterns, further enriching early understanding of fish behaviour.

In the seventeenth century, Giovanni Alfonso Borelli, a disciple of Galileo, made significant strides in the mechanical analysis of fish locomotion. Borelli's work challenged Aristotle's theories, emphasizing the role of body muscles in propulsion and questioning the significance of fins for forward movement [5]. Despite Borelli's contributions, his description of the tail's movement as resembling a frog's foot was later discredited by subsequent research.

Further advancements in understanding fish locomotion came with the pioneering work of Pettigrew in the nineteenth century [6]. Pettigrew critically analysed Borelli's theories, particularly challenging the notion that lateral tail movement alone could produce forward motion. His observations led to a deeper comprehension of the complex interactions between body movements and propulsion forces during fish swimming.

The arrival of cinematography in the late nineteenth century, notably utilized by Etienne-Jules Marey, revolutionized the study of fish locomotion by enabling precise observation and documentation of swimming movements. Marey's sequential photographs provided valuable insights into the wave-like propagation of body curvature during fish locomotion, laying the groundwork for further experimental studies.

In the twentieth century, researchers like Breder and Sir James Gray made significant contributions to the field of fish locomotion. Breder's synthesis on the mechanical principles of fish locomotion categorized various swimming movements and introduced terminology still in use today [7]. Gray's mathematical analyses of fish swimming movements shed light on the hydrodynamics of propulsion, leading to the formulation of Gray's Paradox [8], which continues to stimulate research and debate.

Despite these advancements, bridging the gap between scientific knowledge and fish behaviour remains a formidable challenge. Ongoing research efforts, including mathematical modelling and experimental studies [9–11], hold promise for unravelling the mysteries of fish locomotion and gaining deeper insights into the fascinating world of aquatic movement.

1.2 Modes of Swimming

Breder and Lindsey [7, 12] contributed significantly to the classification and description of fish swimming modes. They distinguished between two primary propulsion modes: swimming locomotion and non-swimming locomotion.

The most common fish swimming modes can be summarized based on two factors: the type of propulsion (undulatory or oscillatory) and the body structures or fins involved in generating thrust. Many fish generate thrust using their body and/or caudal fin (BCF). On the other hand, some fish employ their median and/or paired fins (MPF) while keeping their body relatively rigid. Reviews have indicated that BCF modes are more efficient than MPF modes. However, MPF modes are known for their high manoeuvrability, enabling fast starts, short-radius turning, and other agile movements.

1.2.1 Body and/or Caudal Fin Propulsion

The classification of modes of propulsion by the body or tail has since been somewhat expanded from that designed by Breder and is presented in figure 1.5.

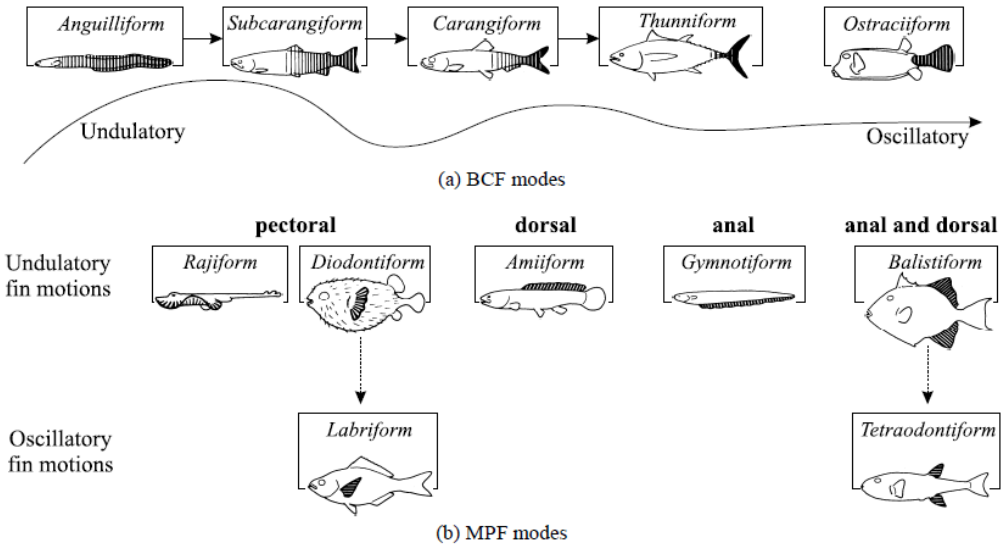

Figure 1.1: Swimming modes associated with (a) BCF propulsion and (b) MPF propulsion. Shaded areas contribute to thrust generation, from [13].

Anguilliform Mode

Anguilliform swimming is a form of locomotion in fish where the entire body, rather than just the tail, undulates in a wave-like motion from head to tail. This swimming mode is typical of elongated, flexible-bodied fish like eels. The movement is characterized by large side-to-side waves that grow in amplitude toward the tail, allowing the fish to propel itself forward. This type of swimming is widespread, especially

among fish species that live near the bottom of aquatic environments, such as flatfish and some species of catfish and sharks.

In anguilliform swimming, the body muscles contract on one side while relaxing on the other, creating a bending wave that travels backward, pushing the fish forward. Although effective for movement, this swimming mode is not particularly fast or energy-efficient compared to other types of fish locomotion. Fish like the Greenland halibut and some cusk-eels exhibit variations of this swimming style, adapting it to different environments, whether close to the seabed or in open water.

The efficiency of anguilliform swimming is influenced by the shape and structure of the fish's body and fins. Fish with bodies that taper towards the tail are generally less efficient swimmers in this mode, while those with a consistent body span or enhanced fins perform better. In some species, like certain sharks and catfish, the anguilliform mode blends into a more powerful swimming style known as subcarangiform, which involves less body movement and a more prominent use of the tail fin.

Overall, anguilliform swimming is a flexible and widespread method of movement among various fish species, particularly those with elongated bodies, although it is not the fastest or most efficient form of locomotion in the aquatic world.

Subcarangiform Mode

Subcarangiform swimming, seen in fish like trout, is similar to anguilliform swimming but differs in that the undulatory motion primarily affects the posterior half or third of the body, with minimal movement at the front. The fish's snout oscillates slightly, and the entire body moves in a sinuous path through the water. Unlike in anguilliform swimming, the amplitude of the undulations remains constant at moderate and high speeds, regardless of the fish's size, with changes in speed achieved by altering the wave's velocity and the tail beat frequency. The tail beat frequency is inversely related to the size of the fish.

Subcarangiform swimmers typically have heavier and more rounded bodies at the front, a deep caudal peduncle, and a caudal fin with a low aspect ratio. This fin is flexible and equipped with intrinsic muscles, allowing it to adjust its area by up to 10% during each beat. This flexibility, combined with a deeper tail at higher speeds, allows for precise control of thrust and manoeuvrability, though the exact mechanisms are complex and not fully understood. Notably, even without the caudal fin, these fish can swim straight, suggesting that the fin evolved more for acceleration, turning, and manoeuvring at high speeds.

Fish like cods have multiple dorsal and anal fins separated by narrow gaps that fill with vortex sheets during swimming, creating a hydrodynamic effect similar to a continuous surface, making their subcarangiform swimming more like anguilliform. In other species, shorter or discontinuous fins help minimize body yaw caused by lateral tail beats, enhancing stability.

Carangiform Mode

Carangiform swimming is a type of locomotion where only the posterior third of a fish's body is involved in generating thrust. This mode of swimming is faster and more efficient than anguilliform swimming because it focuses the undulatory motion in the rear, minimizing energy loss through lateral water displacement and vortex formation. The tail, which is relatively stiff, plays a crucial role in propelling the fish forward, and the undulations are confined to the tail region.

To swim efficiently in the carangiform mode, several adaptations are necessary. Since lateral movements are concentrated at the posterior, these movements create forces that could cause the body to recoil, wasting energy. Fish minimize this recoil by rapidly increasing the wave amplitude near the caudal peduncle, which is narrowed, a feature known as "narrow necking." This allows the body to resist sideways forces, focusing the movement at the tail. Additionally, carangiform fish have a more massive and deeper body towards the front, which, along with stiff median fins, helps stabilize the fish and prevent unwanted side-to-side movement.

The caudal fin in carangiform swimmers is stiff and usually has a V-shaped notch in the center, allowing it to generate a powerful backward thrust as it moves side to side. The high aspect ratio of the tail (long span relative to area) further enhances thrust efficiency. Unlike in subcarangiform swimmers, the caudal fin's movements are not significantly controlled by intrinsic muscles; instead, the fin is manipulated by the trunk and peduncle muscles to maintain an optimal angle for propulsion.

Carangiform swimming is seen in various species, from the moderate forms like Clupeidae (e.g. herring) with less pronounced narrow necking, to more extreme forms like Carangidae (e.g. jacks and mackerels) with deep V-shaped tails. Some species in the Scombridae family (e.g., mackerels and tunas) even approach the thunniform mode, which is characterized by even more extreme adaptations for high-speed swimming.

Unique among these swimmers are the Mormyridae, freshwater fish with electric sensory organs, which have a specialized anatomy that supports carangiform swimming. Their rigid body section, reinforced by bones and tendons, helps stabilize the fish during swimming, likely to maintain the functionality of their electric sensory system rather than to enhance swimming speed.

Thunniform Mode

Thunniform swimming is characterized by thrust generation primarily through the caudal fin, which is mounted on a narrow peduncle, with minimal lateral movement restricted to the peduncle and tail fin. This mode of swimming is extremely efficient and is seen in the fastest marine animals, like tunas and some species of sharks. The fish's body remains largely rigid, with propulsion delivered by massive body muscles to the caudal fin via a sophisticated system of tendons that function like pulleys, passing through two key joints in the posterior vertebral column.

In thunniform swimmers, the body is highly streamlined, with significant mass concentrated in the anterior, often resulting in an almost circular cross-section. The caudal peduncle is extremely narrow and reinforced with lateral keels, which make

it wider than it is deep, aiding in the efficient transfer of force from the body to the caudal fin. The caudal fin itself is high, short in length, and lunate (crescent-shaped), with a very high aspect ratio, resembling the high aspect-ratio wings of birds. This design minimizes drag and maximizes thrust efficiency, allowing these animals to reach and sustain high speeds.

The double-jointed peduncle is crucial to the thunniform mode. The prepeduncular joint allows the peduncle to swing widely, while the postpeduncular joint acts as a hinge, enabling the stiff caudal fin to move effectively. This movement is finely controlled by the deep-seated tendons, such as the posterior oblique tendon and the great lateral tendon, which operate the peduncle and caudal fin. The skin around the peduncle is reinforced with collagenous fibers, preventing the tendons from bowstringing away during the powerful movements of swimming.

Unlike other swimming modes, in thunniform swimmers, the caudal fin leads during lateral beats, with the tips following, providing a consistent backward thrust. The intrinsic muscles of the caudal fin are reduced, and the fin rays overlap the skeletal base, which limits the span but maintains the stiffness necessary for effective propulsion.

Thunniform swimming is seen across various groups, showing remarkable convergence. Besides tunas and some sharks, marine mammals like whales and dolphins, and extinct marine reptiles like ichthyosaurs, also exhibit this swimming mode. These animals share a streamlined body, a lunate tail, and adaptations like narrow necking, despite differences in tail orientation (vertical in fish, horizontal in mammals). The convergence between some sharks and scombroid fishes (like tunas) is particularly notable, with both groups evolving similar shapes and swimming mechanisms.

This mode allows these animals to maintain high speeds over long distances, making them some of the most formidable predators in the ocean.

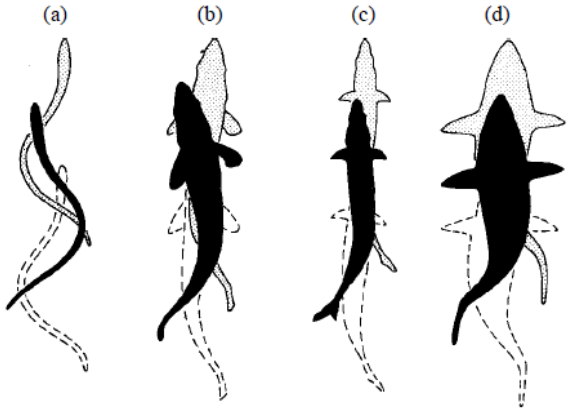

Figure 1.2: BCF swimming modes: (a) anguilliform, (b) subcarangiform, (c) carangiform and (d) thunniform mode.

Ostraciiform Mode

Ostraciiform swimming involves a rigid body that cannot flex laterally, with propulsion driven by a side-to-side oscillation of the caudal fin, similar to a pendulum. This motion is produced by simultaneous muscle contractions on each side of the body. Because the body is inflexible, only the tail moves, resulting in slow, inefficient swimming.

This mode is common in fish like boxfishes, puffers, and porcupinefishes, where the body is often encased in bony armor. These fish mainly use their dorsal and anal fins for slow swimming, with the tail used for quicker movements. The electric ray Torpedo nobiliana also swims in a similar manner, using its caudal fin for propulsion due to its wide, inflexible body. The scabbardfish (Aphanopus carbo) uses an ostraciiform mode when stalking prey, sculling its caudal fin to minimize disturbance. For rapid movement, it switches to undulating its entire body.

Ostraciiform swimmers are generally slower and less streamlined than other swimmers like those using thunniform or carangiform modes. Despite its simplicity, the specifics of ostraciiform swimming in various species are not fully understood.

1.2.2 Median or Pectoral Fins

Fish can achieve propulsion by undulating long-based fins, a method similar to the undulating motion seen in anguilliform body movements. Instead of the body bending, muscles at the base of the fin rays contract, causing the fin rays to move independently. These rays are connected by a flexible membrane, allowing for controlled undulations.

Compared to body undulations, the amplitude of fin undulations is limited since the rays are attached to the body. However, the wavelengths can be short, with multiple waves present on a single fin, and the frequency of these waves can be high up to 70 Hz in a seahorse's dorsal fin.

This type of propulsion allows for lower speeds but offers greater manoeuvrability and precision. Fish can move forward and backward, reverse direction quickly without turning, and hover or drift accurately. Fin undulation keeps the body straight, which is crucial for species with rigid bodies or those that rely on electrosensory or lateral line systems.

The swimming modes categorized by Breder based on fin usage share similar hydrodynamic principles, whether the undulations occur along the dorsal fin, anal fin, or both.

1.3 What is CFD

Computational Fluid Dynamics (CFD) is an interdisciplinary field combining physics, flow technology, programming, mathematics, and mechanics. It involves techniques used to solve the Navier-Stokes equations (typically the Reynolds-Averaged Navier-Stokes equations) to predict fluid behaviour by ensuring the conservation of mass, momentum, and energy. CFD is a valuable tool for exploring physical system designs, performance variables, and diagnosing system behaviour.

CFD is particularly useful when numerous design variations need analysis or when physical testing is impractical due to constraints like scale, cost, accessibility, or environmental risks. It is most effective in situations where modelling has been previously validated or where validation data is readily available. The adoption of CFD has been driven by business and legislative demands for technological advancement and efficiency improvements, alongside the growing accessibility of relevant knowledge and techniques.

Computational Fluid Dynamics (CFD) plays a crucial role in the development and optimization of underwater vehicles, enabling accurate predictions and simulations of fluid behavior. By providing detailed insights into hydrodynamic characteristics, CFD allows designers to refine vehicle structures in the early stages, improving efficiency and reducing resource consumption. Its reliability is further underscored by its strong correlation with experimental results, making it an effective alternative for physical testing.

CFD's integration with biomimetic approaches marks an innovative step in underwater vehicle design, combining natural science and engineering to address complex challenges. The core of CFD analysis involves solving the Navier-Stokes equations, as shown below, which describe fluid motion. This process typically involves discretizing the computational domain into small elements, with flow equations solved within each element.

$$\frac{\partial \rho}{\partial t} + \nabla \cdot (\rho \mathbf{u}) = 0 \tag{1.1}$$

$$\frac{\partial \rho \mathbf{u}}{\partial t} + \nabla \cdot (\rho \mathbf{u} \otimes \mathbf{u}) = \rho \mathbf{g} + \nabla \cdot \overset{\leftrightarrow}{\sigma} + \mathbf{F} \tag{1.2}$$

$$\frac{\partial \rho E}{\partial t} + \nabla \cdot (\rho \mathbf{u} E) = \rho \mathbf{u} \mathbf{g} + \nabla \cdot \left(\overset{\leftrightarrow}{\sigma} \cdot \mathbf{u} \right) - \nabla \cdot \mathbf{q} \tag{1.3}$$

$$f(p, V, T) = 0 \tag{1.4}$$

Among various CFD approaches, the Reynolds-Averaged Navier-Stokes (RANS) method is commonly used for simulating turbulent flows, employing turbulence models like k-ω and k-ϵ for enhanced accuracy. The Unsteady Reynolds-Averaged Navier-Stokes (URANS) method extends RANS to account for time-dependent effects, balancing computational efficiency with the ability to simulate unsteady flows. Advanced methods such as Large Eddy Simulation (LES) and Detached Eddy Simulation (DES) offer more detailed turbulence studies, but with higher computational cost. Direct Numerical Simulation (DNS), which resolves all turbulence scales without modelling, provides the most accurate flow predictions but is primarily used for fundamental research due to its computational intensity.

In the present thesis an Eulerian solver is used (*MaPFlow*) which solves the Unsteady Reynolds Averaged Navier Stokes equations (URANS). The solver is 2nd order accurate in space and time; makes use of the Roe approximate Riemann solver for reconstruction; is equipped with preconditioning to handle Low Mach number rows and uses the Spalart Allmaras and the k-ω SST models for turbulence closure.

1.4 Applications of Biomimetics

Autonomous Underwater Vehicles (AUVs) have become increasingly important due to their wide range of applications, such as deep-sea exploration, seabed geological studies, marine resource extraction, and underwater infrastructure maintenance. However, traditional AUV propulsion systems, which rely on propellers, face challenges like high energy consumption, increased resistance, and significant noise pollution, particularly in complex marine environments. To address these issues, scientists have turned to studying the swimming and manoeuvring techniques of aquatic animals. By mimicking these biological propulsion methods, they are developing innovative, biomimetic AUVs that use coordinated movements of the body, pectoral fins, and tail, along with manipulation of water flow. This approach not only improves speed and reduces noise compared to conventional AUVs but also offers remarkable energy efficiency and enhanced manoeuvrability.

Hydrofoil-like Tail Fin Propulsion

Inspired by the propulsion techniques of aquatic organisms, tail-fin flapping has emerged as a promising method for underwater vehicle design. This approach offers significant advantages such as improved propulsion efficiency, enhanced manoeuvrability, flexibility, and the ability to maintain stability in challenging environments. These benefits highlight the potential for creating highly efficient and adaptable underwater vehicles.

Researchers have extensively studied biomimetic propulsion through numerical simulations using hydrofoils that mimic caudal fins [14, 15]. Their studies focus on understanding how various design parameters like flapping frequency, amplitude, and aspect ratio impact propulsion efficiency and dynamic performance.

These studies collectively highlight that the efficiency and fluid dynamics performance of hydrofoil propulsion are influenced by a complex contribution of factors, including hydrofoil shape, motion patterns, and the surrounding fluid environment. For instance, comparing flapping and oscillating mechanisms shows distinct differences in vortex structures and propulsion efficiency depending on the motion patterns.

Furthermore, investigations into various motion parameters such as the Strouhal number, angle of attack, and pitch amplitude reveal the complexities of designing more efficient hydrofoil systems [16–19]. By emulating the motion characteristics of biological organisms and experimenting with new motion paths, such as multi-degree-of-freedom trajectories, researchers are uncovering innovative ways to enhance hydrofoil propulsion efficiency.

Batoid-like Propulsion

Batoids and rays use a unique swimming technique by flapping their pectoral fins, which grants them high efficiency, agility, and precision in movement. Their superior manoeuvrability is achieved through their streamlined bodies and fin movements.

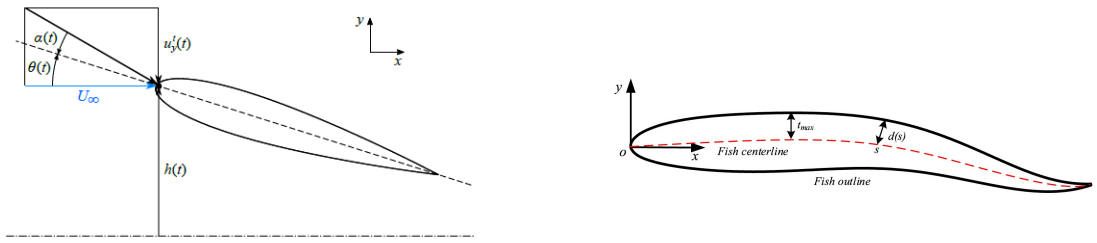

(a) (b)

Figure 1.3: **(a)** NACA0015 foil, from [18]. **(b)** NACA0012 fish-like foil ,from [16]

Researchers use computational fluid dynamics to simulate the hydrodynamic performance of batoids, exploring how factors like motion frequency, amplitude, and thrust affect it [20–23].

In the field of biomimetic modeling, researchers have developed advanced simulations and algorithms to mimic the swimming behavior of batoids. Notable contributions include the development of self-propelled robotic batoid devices, soft material robotic batoids, and designs featuring dual pectoral fins with auxiliary power thrusters [24, 25]. These innovations aim to replicate the efficient and agile swimming mechanisms of batoids in robotic systems.

Overall, all studies provide a thorough comprehension of batoid dynamics and motion mechanisms. By closely examining the swimming techniques of batoids, researchers are able to design more efficient and agile AUVs, advancing the field of biomimetic robotics and offering potential applications in marine engineering and exploration.

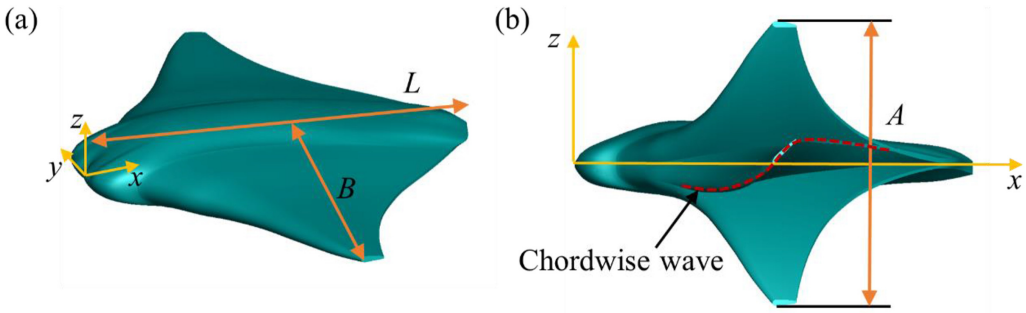

Figure 1.4: A 3D ray model, from [26]

Dolphin Propulsion

Dolphins are renowned for their exceptional swimming efficiency, primarily due to their unique dorsoventral propulsion mechanism. This method, which involves movement from the belly to the back, is common among aquatic mammals and significantly influences how researchers approach the design of underwater vehicles. By emulating dolphins' kinematics, researchers aim to create high-performance underwater robots [27, 28].

The swimming efficiency of dolphins derives from the complex interaction between their body and pectoral, dorsal, and caudal fins. This coordination provides remarkable agility and propulsion power. Understanding these interactions is crucial for enhancing underwater vehicle design and replicating dolphin-like swimming mechanisms.

Recent advancements in dolphin-inspired robotic systems highlight significant progress in simulating dolphin locomotion and improving robotic performance. Xue et al. [29] investigated the C-turning, pitching, and flapping propulsion of dolphin robots, developing a model that enhances manoeuvrability. Cao et al. [30] introduced an elliptical-trajectory pectoral fin oscillation model to refine control precision in various aquatic environments. Wu and his team integrated mechanical dolphin advantages with underwater gliders, improving manoeuvrability, speed, and endurance.

Further studies combined experimental and numerical methods to analyse dolphin thrust generation and wake structure [31–33]. These research efforts contribute to a deeper understanding of dolphin hydrodynamics and CFD applications, offering valuable insights for designing efficient and agile underwater robots. By drawing inspiration from dolphin swimming mechanisms, these studies pave the way for innovative underwater robotic technologies and future advancements in this field.

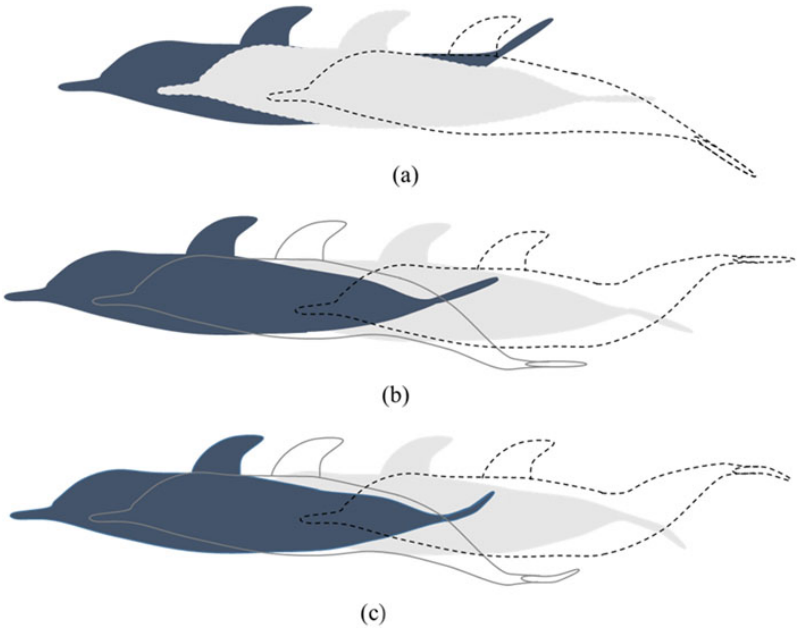

Figure 1.5: The postures of the three propulsion modes during the movement of the dolphin. (a) Single-stage propulsion, (b) Double-stage propulsion, (c) Multi-stage propulsion, from [33]

Drag Reduction

Underwater vehicles face significant drag forces during operation, which can reduce navigation speed, increase energy consumption, and affect overall stability and ma-

noeuvrability. To address these challenges, biomimetic drag reduction technologies, which inspired by aquatic creatures such as shark skin structures and the coordinated movements of fish [34, 35], have been gradually embedded into the design and manufacturing of underwater vehicles so that they don't only have reduced drag but also increased navigation efficiency.

Researchers have drawn inspiration from various marine creatures. For instance, squid-inspired surfaces have shown a 25% reduction in drag, while flounder-based designs demonstrated synergistic effects in minimizing resistance [36, 37]. Similarly, pufferfish spine structures reduced drag by up to 10.6%, and further innovations incorporating pufferfish-inspired elements into copper surfaces enhanced both drag reduction and surface stability [38–40].

In another example, surfaces influenced by dolphins' skin and mosquitoes' mouthparts achieved a remarkable drag reduction of 89.49%. Shark-inspired designs also proved effective, with one study optimizing AUV systems for improved efficiency and docking. Fish scales and seal whiskers inspired additional designs that helped reduce drag and fluid flow vibration [41, 42].

Finally, humpback whale flipper morphology inspired hydrofoil designs that enhanced lift and reduced drag, with reductions of up to 35.13% [43]. Collectively, these studies demonstrate the vast potential of biomimetic approaches in improving underwater vehicle efficiency and advancing marine engineering technologies.

Noise Reduction

Reducing noise remains a significant challenge in the development of underwater vehicles, leading to a growing interest in biomimetic approaches as potential solutions. These methods are inspired from natural designs to enhance vehicle structures, such as using shark skin to minimize drag, adopting the tubercle design of humpback whale flippers for better flow control, and mimicking the serrated edges of owl wings to reduce noise.

In some studies, scientists used tubercles from humpback whale flippers [44], to design a quieter ducted propeller, as shown in Figure 1.6. Using advanced simulations and acoustic modelling, they found that these tubercles reduce noise by disrupting turbulence in the propeller wake, hastening the decay of turbulence and reducing vortex-induced noise. The design was adapted also to propeller blades to mitigate cavitation noise and has applications in both underwater vehicles and aviation [45]. Figure 1.7 shows the form of the propeller blades.

In a noteworthy study, Li et al. carried out numerical simulations to study the effects of a wave-shaped leading edge on the flow structure and noise of hydrofoils [46]. Their findings revealed that this design not only reduced variations in lift and drag but also modified the flow field, effectively minimizing or eliminating tonal noise without greatly influencing noise directivity. The design was especially effective at higher inflow speeds in reducing lift fluctuations and noise. Finally, in another study, Dang et al. developed a transverse micro-groove surface, as shown in Figure 1.8, inspired by shark skin, to further reduce noise in underwater vehicles [47]. Using numerical simulations and experimental data, they showed that the micro-groove surface decreased hydrodynamic noise by up to 7.28 dB, as the grooves generated

secondary vortices that disrupted turbulence and reduced its intensity.

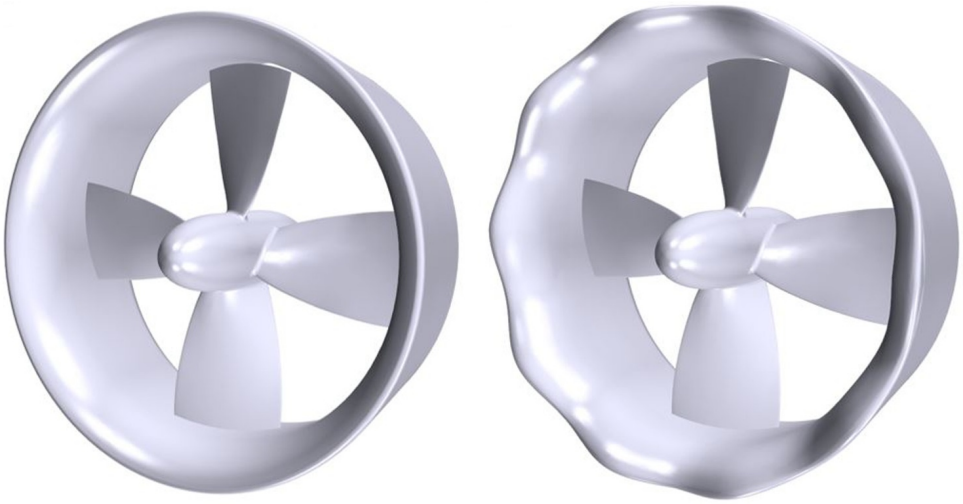

Figure 1.6: Biomimetic ducted propeller geometry, from [44]

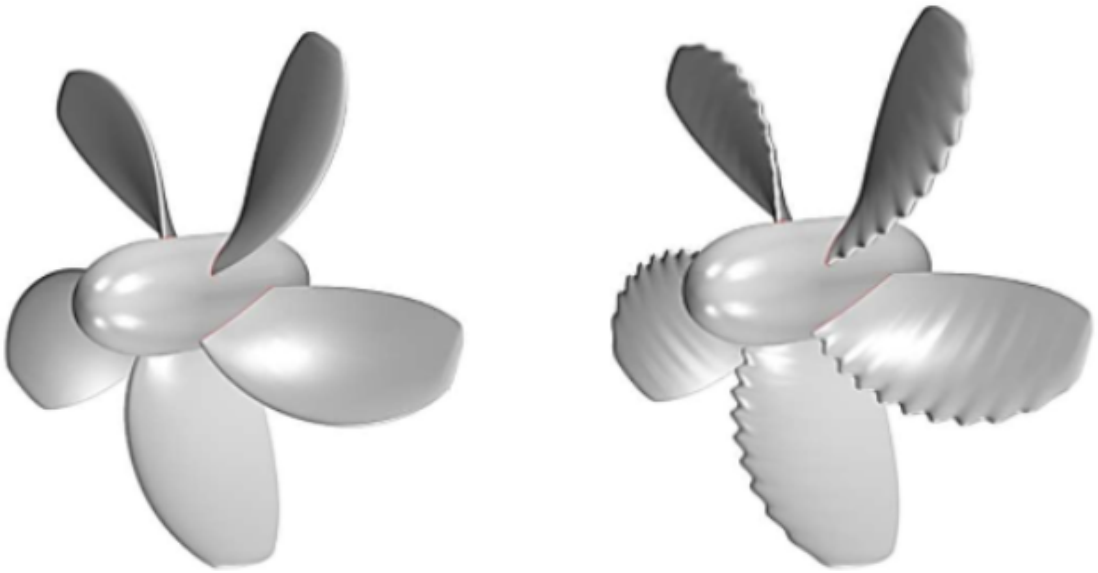

(a) (b)

Figure 1.7: (a) Basic propeller, (b) Tubercle propeller, from [44]

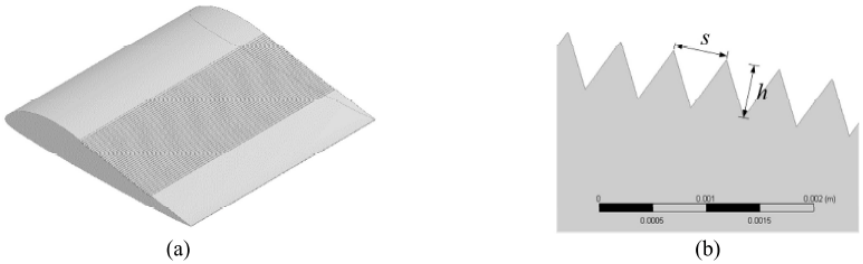

Figure 1.8: Three-dimensional hydrofoil partially covered with micro-grooves: (a) overall model and (b) details of the microgrooves, from [47]

This page is intentionally left blank.

Chapter 2

Methodology

2.1 Governing Equations

The Navier-Stokes equations, which describe the motion of fluids, as know in the previous chapter are:

$$\frac{\partial \rho}{\partial t} + \nabla \cdot (\rho \mathbf{u}) = 0 \tag{2.1}$$

$$\frac{\partial \rho \mathbf{u}}{\partial t} + \nabla \cdot (\rho \mathbf{u} \otimes \mathbf{u}) = \rho \mathbf{g} + \nabla \cdot \overset{\leftrightarrow}{\sigma} + \mathbf{F} \tag{2.2}$$

$$\frac{\partial \rho H}{\partial t} + \nabla \cdot (\rho \mathbf{u} H) = \rho \mathbf{u} \mathbf{g} + \nabla \cdot \left(\overset{\leftrightarrow}{\sigma} \cdot \mathbf{u} \right) - \nabla \cdot \mathbf{q} \tag{2.3}$$

$$f(p, V, T) = 0. \tag{2.4}$$

Incompressible Viscous flow

In the case of incompressible viscous flows, the equations describing the fluid's motion are the mass and momentum conservations:

$$\partial_j u_j = 0, \quad \text{and} \tag{2.5}$$

$$\partial_t u_i + u_j \partial_j u_i = -\frac{1}{\rho} \partial_i p + \nu \Delta u_i + F_i \tag{2.6}$$

Conservative Form

To obtain the discrete system, we refer back to the conservative form together with the transport equation for the volume fraction.

$$\partial_j u_j = 0 \tag{2.7}$$

$$\frac{\partial (\rho u_i)}{\partial t} + \partial_j (\rho u_i u_j) + \partial_i p = \partial_j \sigma_{ij} + F_{Bi}, \quad i = 1, 2, 3 \tag{2.8}$$

Applying the Green-Gauss theorem and integrating over a control volume, we get:

$$\int_{D_k} \partial_j u_j \, dD_k = 0 \tag{2.9}$$

$$\frac{\partial}{\partial t} \int_{D_k} \rho_m u_i \, dD_k + \int_{D_k} \partial_j \left(\rho_m u_i u_j \right) \, dD_k + \int_{D_k} \partial_i p \, dD_k = \int_{D_k} \partial_j \sigma_{ij} \, dD_k + \int_{D_k} F_{Bi} \, dD_k \tag{2.10}$$

Introducing the outward normal vector $\vec{n}$ and applying the Green-Gauss theorem, one gets:

$$\int_{\partial D_k} u_j n_j \, ds_k = 0 \tag{2.11}$$

$$\frac{\partial}{\partial t} \int_{D_k} \rho u_i \, dD_k + \int_{\partial D_k} \rho u_i \left(u_j n_j \right) \, ds_k + \int_{\partial D_k} n_j p \, ds_k = \int_{\partial D_k} \sigma_{ij} n_j \, ds_k + \int_{D_k} F_{Bi} \, dD_k \tag{2.12}$$

Presenting the above in a vector form and performing the variable transformation to the primitive variables, gives:

$$\Gamma \frac{\partial \bar{Q}}{\partial t} + \int_{\partial D_k} \bar{Q} \left(\bar{F}_c - \bar{F}_v \right) ds_k = \int_{D_k} \bar{S} dD_k \tag{2.13}$$

$$U = \begin{bmatrix} 0 & \rho u & \rho v & \rho w \end{bmatrix}^T, \quad Q = \begin{bmatrix} p & u_i \end{bmatrix}^T$$

$$\frac{\partial \bar{U}}{\partial t} = \frac{\partial \bar{U}}{\partial \bar{Q}} \frac{\partial \bar{Q}}{\partial t} = \Gamma \frac{\partial \bar{Q}}{\partial t} \tag{2.14}$$

$$\Gamma = \begin{bmatrix} 0 & 0 & 0 \\ 0 & \rho \bar{I}_{3\times 3} & \mathbf{u_i} \Delta \rho \\ 0 & 0 & 1 \end{bmatrix} \tag{2.15}$$

$$\bar{F}_c = \begin{bmatrix} V_n \\ \rho u V_n + p n_x \\ \rho v V_n + p n_y \\ \rho w V_n + p n_z \\ 0 \end{bmatrix}$$

$$\bar{F}_v = \begin{bmatrix} 0 \\ \tau_{xx} n_x + \tau_{xy} n_y + \tau_{xz} n_z \\ \tau_{yx} n_x + \tau_{yy} n_y + \tau_{yz} n_z \\ \tau_{zx} n_x + \tau_{zy} n_y + \tau_{zz} n_z \\ 0 \end{bmatrix}$$

where $V_n = \bar{\mathbf{u}} \cdot \bar{\mathbf{n}}$.

2.2 Artificial Compressibility

The Artificial Compressibility method was invented by Chorin in 1967 [48] and its purpose is to deal with the decoupling of mass and momentum conservation equations by introducing to the former a pseudo-time derivative of this pressure. Doing so, one can leverage techniques and algorithms used for compressible flows to solve incompressible flow problems. The AC method suggests a relation between density and pressure:

$$\frac{\partial \rho}{\partial p} = \frac{1}{\beta} \tag{2.16}$$

Combining the above equation with the mass equation we get:

$$\frac{1}{\beta}\partial_\tau p + \partial_j u_j = 0 \tag{2.17}$$

where τ is the pseudo-time variable, β is the AC factor and p is the pressure. Eq.2.17 result in a single coupled system of equations, accompanied by the relevant boundary conditions, which can be solved using an iterative approach. The artificial compressibility factor, β, is an adjustable numerical parameter that must be chosen independently. Higher values of β cause a weaker coupling of the equations, leading to slower convergence. For single-phase flows, typical β values range from 5 to 100.

2.3 Definition of a Control Volume

Space is divided into a set of unstructured computational cells. The center of each control volume is located at the geometric center of the corresponding computational cell. Figure 2.1 shows an example of a 2-D control volume.

Before discretizing the equations, the geometric properties of the cells must be calculated. Starting with face calculations, each face generally forms a polygonal area, and a common method is to triangulate the face. The area and geometric center of each triangle are then computed. The total area of the polygonal face is obtained by summing the subareas of the triangles, and its center is determined as the geometric mean of the triangle centers [49].

The center of each computational cell is the geometric mean of its vertices, represented as:

$$\vec{x}_{ci} = \frac{1}{N_v}\sum_{v=1}^{N_v} \vec{x}_{vj} \tag{2.18}$$

where $\vec{x}_{ci}$ is the center of the i^{th} computational cell, N_v is the total number of vertices defining the control volume, and $\vec{x}_{vj}$ are the positions of these vertices.

To calculate the cell's volume, the Green-Gauss theorem is applied. By defining the function $\vec{F} = (0, 0, z)$ and since $\nabla \cdot F = 1$, the total volume of a computational cell can be calculated as:

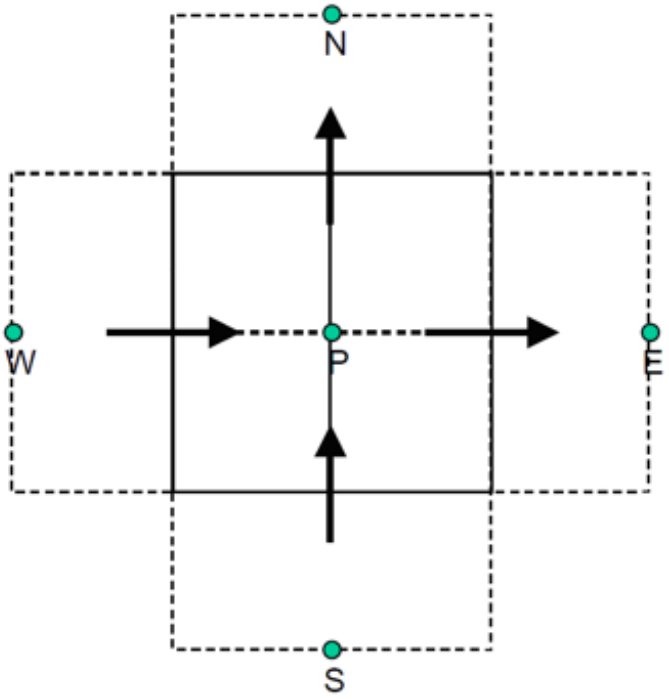

Figure 2.1: A 2-D control volume.

$$V_i = \sum_{f=1}^{N_f} z_f n_{zf} S_f \tag{2.19}$$

where, V_i is the volume of the i^{th} cell, z_f is the z-coordinate of the midpoint of face f and n_{zf} the z-component of the normal of that face.

Noticeable most of the computational cells are not water tight. This caused due to the vertices defining a face. In most cases the vertices of the same face do not lie on the same plane. This implies that for the faces of a control volume the following condition arises,

$$\sum_{f}^{N_f} \vec{n}_f S_f \neq 0 \tag{2.20}$$

This is the case for the majority of the computational meshes containing faces with more than 3 vertices, but it is more evident in meshes with arbitrary polyhedral volumes. A correction can be applied to Equation (2.19) to account for the non–planar vertices of the mesh. The non-water tight control volumes is a major source of accuracy drop in 3D simulations.

2.4 Finite Volume Method

The Finite Volume Method (FVM) is a computational technique used to transform partial differential equations (PDEs) that represent conservation laws into algebraic

equations over finite volumes. Similar to the finite difference and finite element methods, FVM starts by dividing the geometric domain into non-overlapping finite volumes. The PDEs are then integrated over these volumes and converted into algebraic equations, which are solved to determine the dependent variable values for each volume. In FVM, certain terms in the conservation equations are converted into face fluxes and evaluated at the boundaries of the finite volumes. This ensures that the flux entering one volume equals the flux leaving the adjacent volume, making FVM strictly conservative. This conservation property makes FVM particularly favored in computational fluid dynamics (CFD).

Introducing the pseudo-time term in eq. 2.13 we get the following:

$$\Gamma_\tau \frac{\partial}{\partial \tau} \int_{\partial D_k} \mathbf{Q}\, dD_k \Gamma \frac{\partial \bar{Q}}{\partial t} + \int_{\partial D_k} \bar{Q} \left(\bar{F}_c - \bar{F}_v \right) ds_k = \int_{D_k} \bar{S} dD_k \tag{2.21}$$

where

$$\Gamma_\tau = \begin{bmatrix} \frac{1}{\beta\rho} & 0 & 0 \\ 0 & \rho I_{3\times 3} & \mathbf{u}\Delta\rho \\ \frac{1}{\beta\rho} & 0 & 1 \end{bmatrix} \tag{2.22}$$

2.4.1 Spacial Discretization

In MaPFlow, the flow variables are calculated and stored at cell centers. Assuming that the cell volume remains unchanged:

$$\frac{\partial}{\partial t} \int_D \overline{U} dD = D \frac{\partial \overline{U}}{\partial t} \tag{2.37}$$

where

$$\overline{U} = \frac{1}{D} \int_D U_{exact} dD \tag{2.38}$$

Thus, equation (2.1) becomes:

$$\frac{\partial \overline{U}}{\partial t} = -\frac{1}{D} \left[\int_{\partial D} \left(\vec{F}_c - \vec{F}_v \right) dS - \int_D \vec{Q} dD \right] \tag{2.39}$$

The surface integral is approximated using piecewise constant fluxes over the cell faces that are calculated at their centers. For cell I,

$$\frac{d\overline{U}_I}{dt} = -\frac{1}{D_I} \left[\sum_{m=1}^{N_f} \left(\vec{F}_c - \vec{F}_v \right)_m \Delta S_m - \left(\vec{Q} D \right)_I \right] = -\frac{1}{D_I} \overline{R}_I \tag{2.40}$$

where N_f is the number of faces the cell has and ΔS_m is the area of face "m". The terms $\left(\vec{F}_c \right)_m$, $\left(\vec{F}_v \right)_m$ represent the convective and viscous fluxes through face m.

Reconstruction of faces

In order to account for the different features of the flow variables, different reconstruction strategies are adopted for each one of them.

Firstly, for the velocity field, a piece-wise linear reconstruction (PLR) scheme is used that extrapolates the cell center values of the neighboring cells i, j at the corresponding left (L) and right (R) states. More precisely, in Figure 2.2, two neighboring cells i, j, with a common boundary f, are illustrated. The two cells have volumes Ω_i and Ω_j, respectively. The face f is defined based on the normal vector $\vec{n}$. The known values at the cell centers need to be extrapolated to the states L and R. The velocities $\vec{v}_L$ and $\vec{v}_R$ can be approximated using a second-order Taylor expansion as:

$$\begin{aligned} \mathbf{u_L} &= \mathbf{u_i} + \nabla \mathbf{u_i} \cdot \mathbf{r_i} \\ \mathbf{u_R} &= \mathbf{u_j} + \nabla \mathbf{u_j} \cdot \mathbf{r_j} \end{aligned} \tag{2.23}$$

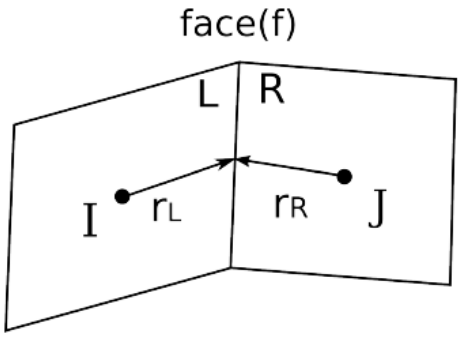

Figure 2.2: Reconstruction of variables on the faces.

As for the inviscid fluxes $\mathbf{F_c}$, the approximate Riemann solver of Roe is used [**spacial**].

$$\mathbf{F_{c,f}} = \frac{1}{2}\left(\mathbf{F_c}\left(\mathbf{Q_R}\right) + \mathbf{F_c}\left(\mathbf{Q_L}\right)\right) - \frac{1}{2}|\Gamma \mathbf{A_{c,f}}|\left(\mathbf{Q_R} - \mathbf{Q_L}\right) \tag{2.37}$$

Where $\mathbf{A_c}$ is the preconditioned Jacobian Matrix.

$$\mathbf{A_c} = \frac{\partial \mathbf{F_c}}{\partial \mathbf{Q}} = \Gamma\Gamma^{-1}\mathbf{A_c} = \Gamma \mathbf{A_c} \tag{2.24}$$

Where Γ is the precondition matrix given by Kunz et al [50]. For viscous fluxes, a simple cell-averaged value is used.

2.4.2 Temporal Discretization

For every time true computational step a pseudo-steady problem is solved. Let $\mathbf{Q}$ be the flow variables that are used to solve the pseudo-steady time problem, which until convergence they do not satisfy the original unsteady problem. At every pseudo-time step iteration k, for a computational cell i, a problem of the form (3.43) is solved:

$$\Gamma_i \Omega_i \frac{\partial \mathbf{Q}_i^*}{\partial \tau} + \mathbf{R}_{u,i} = 0 \tag{2.25}$$

where $\mathbf{R}_{u,i}$ is the unsteady residual of the ith cell, defined as the sum of the spatial residual and the time-derivatives, i.e.

$$\mathbf{R}_{u,i} = \mathbf{R}_i \left(\mathbf{Q}_i^* \right) + \Gamma_e \frac{\partial \left(\Omega_i \mathbf{Q}_i^* \right)}{\partial t} \tag{2.26}$$

The convergent solution of the problem is obtained when $\mathbf{R}_{u,i} \to 0$ and thus $\mathbf{Q}^* \to \mathbf{Q}^{n+1}$ (n is the time marching iterator). In case of steady flow problems the unsteady residual is equal to the spatial, since the unsteady term is omitted. In this case, the pseudo-time marching begins with $k = 0$ and the convergent steady solution of the problem is obtained once the pseudo-time derivatives tend to zero.

A fully implicit scheme is used for the discretization of the unsteady terms. Let $n+1$ be the unknown time level, with the flow quantities being known for the time levels $n, n-1, n-2, \ldots$, writing the time derivative as a series expansion of successive levels backward in time, the following backwards difference formula (BDF) is obtained,

$$\frac{\partial \left(\Omega_i \mathbf{Q}_i^* \right)}{\partial t} = \frac{1}{\Delta t} \left[\varphi_{n+1} \left(\Omega_i \mathbf{Q}_i^* \right)^{n+1} + \varphi_n \left(\Omega_i \mathbf{Q}_i^* \right)^{n} + \varphi_{n-1} \left(\Omega_i \mathbf{Q}_i^* \right)^{n-1} + \varphi_{n-2} \left(\Omega_i \mathbf{Q}_i^* \right)^{n-2} + \ldots \right] \tag{2.27}$$

By rearranging the terms of the above equation, the discretized unsteady term can be written as:

$$\frac{\partial \left(\Omega_i \mathbf{Q}_i \right)}{\partial t} = \frac{1}{\Delta t} \left[\left(\mathbf{Q}_i^{n+1} \Omega_i^{n+1} + \varphi_n \mathbf{Q}_i^n \Omega_i^n + \varphi_{n-1} \mathbf{Q}_i^{n-1} \Omega_i^{n-1} + \varphi_{n-2} \mathbf{Q}_i^{n-2} \Omega_i^{n-2} + \ldots \right) + \left(\mathbf{Q}_i^{n+1} - \mathbf{Q}_i^n \right) \right. \tag{2.28}$$

In order to enforce volume conservation, the GCL is imposed on the time discretization process. Using the same sequence of the BDF scheme and assuming constant value fluxes at each face of the cell, Equation (2.16) can be discretized as:

$$\frac{1}{\Delta t} \left[\left(\varphi_{n+1} \Omega_f^{n+1} + \varphi_n \Omega_f^n + \varphi_{n-1} \Omega_f^{n-1} + \varphi_{n-2} \Omega_f^{n-2} + \ldots \right) \right] = \sum_{f=1}^{N_f} \frac{V_{g,f}}{\Delta S} = \mathbf{R}_{gcl}^n \tag{2.29}$$

2.5 Grid Deformation

In computational fluid dynamics (CFD), the interaction between fluid and solid structures necessitates adapting the computational mesh to accommodate moving boundaries. Various applications, such as flutter simulations of wings, blood flow in veins, and stability analysis of structures under wind loads, underscore the importance of efficiently handling dynamic domains.

Traditionally, methods like the deforming mesh approach adjust mesh nodes along solid boundaries to communicate the motion of rigid bodies to the flow solver.

While several techniques have been proposed in the literature to achieve efficient grid deformation with high-quality mesh characteristics, none offer universal applicability across all scenarios.

Mesh deformation technology plays a crucial role in ensuring the accuracy and efficiency of CFD simulations involving moving boundaries. It involves adjusting mesh coordinates without altering topology, thereby avoiding interpolation between different mesh configurations and reducing computational cost.

Efforts are underway to develop fast and reliable algorithms for automatically updating grids in unsteady flow computations. These algorithms aim to overcome the challenges associated with regenerating complex grids at each time step, thereby streamlining the simulation process and improving computational efficiency.

2.5.1 Radial Basis Functions (RBF)

The interpolation scheme used in this thesis is widely applicable, especially in fluid-structure interaction problems. Radial Basis Functions (RBF) are a great method for interpolating scattered data. In this method, each wall node is assigned an area of influence, where the movement of the internal mesh nodes is determined by a weighting factor. The displacement $s(\mathbf{x})$ of an internal mesh node is described by an interpolation function, which consists of a sum of basis functions $\phi(\cdot)$, along with a polynomial function $p(x)$ to account for mesh rotation. These basis functions are defined at each wall node s_i.

Given N number of interpolating points the radial basis function is written as:

$$\phi_{s_i}(\mathbf{x}) = \phi(\|\mathbf{x} - \mathbf{x_{s_i}}\|) \tag{2.30}$$

where, $\|\cdot\|$ is the Euclidean norm and $\mathbf{x_{s_i}} = [x_{s_i}, y_{s_i}, z_{s_i}]$ are the known boundary value displacements. The interpolation function is constructed as a sum of basis functions:

$$s(\mathbf{x}) = \sum_{i=1}^{N} \alpha_i \phi(\|\mathbf{x} - \mathbf{x_{s_i}})\|) + p(\mathbf{x}) \tag{2.31}$$

where $p(\mathbf{x})$ is a polynomial whose degree depends on the choice of the basis function ϕ [51]. The polynomial $p(\mathbf{x})$ is determined by the coefficients α_i, which are found by evaluating the interpolation function $s(\mathbf{x})$ at the specified boundary points:

$$s(\mathbf{x}) = \Delta x_{s_i}, \tag{2.32}$$

where Δx_{s_i} contains the known discrete values of the boundary point displacements, combined with the additional requirement:

$$\sum_{i=1}^{N} \alpha_i q(\mathbf{x}) = 0 \tag{2.33}$$

which is true for all polynomials $q(\mathbf{x})$ with degree less or equal than that of $p(\mathbf{x})$.

To calculate the values of the coefficients α_i and the coefficients of polynomial $p(\mathbf{x})$ one must solve the following linear system:

$$\begin{bmatrix} \Delta \mathbf{x_{s_i}} \\ \mathbf{0} \end{bmatrix} = \begin{bmatrix} C_{ss} & \mathbf{M_{s_i}} \\ \mathbf{M_{s_i}}^T & \mathbf{0} \end{bmatrix} \begin{bmatrix} \gamma \\ c \end{bmatrix} \tag{2.34}$$

where γ contains all coefficients γ_j, c the coefficients of the polynomial $p(x)$, C_{ss} an $s_N \times s_N$ matrix contains the evaluation of the basis function $\phi_{s_i s_j} = \phi(\|\mathbf{x_{s_i}} - \mathbf{x_{s_j}}\|)$ and can be seen as a connectivity matrix connecting all boundary points with every other boundary point. $\mathbf{M_b}$ is an $(s_N \times 4)$ matrix with row j given by $[1\ \mathbf{x_{s_j}}]$.

After the coefficients in γ and c have been obtained, they are used to calculate the values for the displacements of all internal fluid points $\Delta \mathbf{x_{in_j}}$, using the evaluation function:

$$\Delta \mathbf{x_{in_j}} = s(\mathbf{x_{in_j}}). \tag{2.35}$$

2.6 Turbulence

Nearly all fluid flow we encounter in everyday life is turbulent. Common examples include the flow around and inside cars and airplanes, the water in a river, the smoke from a chimney. The boundary layer of the earth's atmosphere is turbulent. Chemical engineers utilize turbulence to mix and homogenize fluid mixtures, as well as to speed up chemical reactions in fluids and gases. Although, at first glance, turbulence may seem chaotic or random, its study is a multidisciplinary task which has a variety of applications. Nevertheless, it is very challenging to define turbulence precisely, but there some characteristics of turbulence flow that can be specified[**turb**].

Irregularity. Turbulent flow is characterized by its irregularity, randomness, and chaotic nature. It comprises a range of scales (eddy sizes), with the largest eddies being comparable to the dimensions of the flow geometry and the smallest eddies are dissipated into internal energy by viscous forces. Despite its chaotic appearance, turbulence is deterministic and governed by the Navier-Stokes equations.

Diffusivity. In turbulent flow, diffusivity increases, enhancing the exchange of momentum, delaying flow separation around bluff bodies. Diffusivity also increases resistance and heat transfer rates.

High Reynolds numbers. Turbulent flows always occur at high Reynolds numbers. Turbulence typically starts as an instability in laminar flows when the Reynolds number becomes too large. These instabilities arise from the interaction between viscous terms and nonlinear inertia terms in the equations of motion.

Three-dimensional vorticity fluctuations. Turbulence is rotational and three-dimensional, characterized by high levels of fluctuating vorticity. The random vorticity fluctuations of turbulence could not sustain themselves if the velocity fluctuations were only two-dimensional, because vortex stretching, an essential vorticity-maintenance mechanism, is absent in two-dimensional flows.

Dissipation. Turbulent flows are always dissipative, with viscous shear stresses doing deformation work that increases the fluid's internal energy at the cost of the turbulent kinetic energy.

Continuum. Turbulence is a continuum phenomenon described by fluid mechanics equations. Even the smallest turbulent scales are much larger than any

molecular length scale.

2.6.1 Turbulence Modelling

Turbulence modelling involves creating a set of partial differential equations to calculate turbulent flow, using approximations of the exact Navier–Stokes equations. In this thesis the Reynolds-averaged Navier–Stokes equations (RANS) approach is used and begins by decomposing the flow variables into mean and fluctuating components. When these decomposed variables are inserted into the Navier–Stokes equations and averaged, the result is the Reynolds-stress tensor, an unknown term that must be modelled to solve the RANS equations. This process essentially addresses the closure problem of the Navier–Stokes equations system.

Reynolds-Averaged Navier-Stokes equations

Reynolds decomposition begins with the dependent variables being decomposed into a mean and a fluctuating part:

$$u_i = \overline{u_i} + u_i' \tag{2.36}$$

where:

$$\overline{u_i} = \lim_{T\to\infty} \frac{1}{T} \int_t^{t+T} u_i \, dt \tag{2.37}$$

with the following assumed properties:

$$\overline{u_i'} = \overline{u_j'} = 0 \tag{2.38}$$

$$\overline{u_i u_j} = \overline{u_i}\,\overline{u_j} + \overline{u_i' u_j'}, \tag{2.39}$$

$$\overline{\overline{u_i} u_i'} = \overline{\overline{u_j} u_j'} = \overline{\overline{u_i} u_j'} = \overline{\overline{u_j} u_i'} = 0, \tag{2.40}$$

$$\overline{u_i^2} = \overline{u_i}^2 + \overline{u_i'^2}, \tag{2.41}$$

$$\overline{\frac{\partial u_i}{\partial t}} = \frac{\partial \overline{u_i}}{\partial t}, \qquad \overline{\frac{\partial u_i}{\partial x_i}} = \frac{\partial \overline{u_i}}{\partial x_i} \tag{2.42}$$

To derive the system of partial differential equations governing the mean-velocity and pressure fields in incompressible turbulent flow, one must substitute Eq. (2.36) into the Navier-Stokes equations,take an ensemble average and enforce the above properties [52]:

$$\frac{\partial \overline{u_i}}{\partial x_i} = 0 \tag{2.43}$$

$$\frac{\partial \overline{u_i}}{\partial t} + \overline{u_j}\frac{\partial \overline{u_i}}{\partial x_j} = -\frac{1}{\rho}\frac{\partial \overline{p}}{\partial x_i} + \nu\frac{\partial^2 \overline{u_i}}{\partial x_j^2} - \frac{\partial \tau_{ij}}{\partial x_j} \tag{2.44}$$

where

$$\tau_i j = \overline{u_i' u_j'} \tag{2.45}$$

is the Reynolds-stress tensor divided by the density.

Additional equations are required for the closure of the problem. The eddy hypothesis. also known as Boussinesq approximation, is a standard approach used to compute the Reynolds stresses. The hypothesis states that Reynolds stress can be calculated similarly to normal stress but with a variable viscosity, known as turbulent viscosity. This turbulent viscosity must be determined using an appropriate turbulence model. The hypothesis states that:

$$\tau_{ij} = 2\nu_T \left(S_{ij} - \frac{2}{3}\frac{\partial u_k}{\partial x_k}\delta_{ij} \right) - \frac{2}{3}k\delta_{ij} \tag{2.46}$$

where:

$$S_{ij} = \frac{1}{2}\left(\frac{\partial \overline{u_i}}{\partial x_j} + \frac{\partial \overline{u_j}}{\partial x_i} \right) \tag{2.47}$$

is the stress tensor,

$$k = \frac{1}{2}\overline{u_i' u_i'}$$

is the turbulent kinetic energy, $\nu_T = \mu/\rho_T$ is the turbulent viscosity (or eddy viscosity) and δ_{ij} is the Kronecker delta.

2.6.2 Menter's k-omega SST model

Menter in [53] used a hybrid model in order to achieve desired features in all the different regions. He uses the Wilcox k-omega formulation [54] near the wall and the k-ϵ model in the outer part of the boundary layer in order to exploit its freestream independence. The k-ϵ model is transformed into a k-omega formulation and multiplied by $(1 - F_1)$, where F_1 is blending function designed to be one near the wall and zero away from the surface of the wall. Then, the Wilcox k-omega is multiplied by F_1 and added to the previous equations. The resulting equations are:

$$\frac{D\rho k}{Dt} = \tau_{ij}\frac{\partial u_i}{\partial x_j} - \beta^* \rho\omega k + \frac{\partial}{\partial x_j}\left[\left(\mu + \sigma_k \mu_T \right) \frac{\partial k}{\partial x_j} \right] \tag{2.48}$$

$$\frac{D\rho\omega}{Dt} = \frac{\gamma}{\nu_T}\tau_{ij}\frac{\partial u_i}{\partial x_j} - \beta^* \rho\omega^2 + \frac{\partial}{\partial x_j}\left[\left(\mu + \sigma_\omega \mu_T \right) \frac{\partial \omega}{\partial x_j} \right] + 2\rho\left(1 - F_1\right)\sigma_{\omega 2}\frac{1}{\omega}\frac{\partial k}{\partial x_j}\frac{\partial \omega}{\partial x_j} \tag{2.49}$$

where:

$$\mu_T = \frac{\rho\alpha_1 k}{\max(\alpha_1\omega; \Omega F_2)} \tag{2.50}$$

Every constant ϕ of the SST model can be calculated with the following equation:

$$\phi = F_1\phi_1 + (1 - F_1)\phi_2 \tag{2.51}$$

where ϕ_1 is a constant from Wilcox's model, ϕ_2 from the transformed k-ϵ model and F_1 and F_2 are defined by:

$$F_1 = \tanh(\arg_1^4), \quad \arg_1 = \min\left[\max\left(\frac{\sqrt{k}}{\beta^*\omega d}; \frac{500\nu}{d^2\omega}\right), \frac{4\rho\sigma_2 k}{CD_{k\omega}d^2}\right] \tag{2.52}$$

$$CD_{k\omega} = \max\left(2\rho\sigma_2\frac{1}{\omega}\frac{\partial k}{\partial x_j}\frac{\partial\omega}{\partial x_j}, 10^{-20}\right) \tag{2.53}$$

$$F_2 = \tanh(\arg_2^2), \quad \arg_2 = \max\left(2\frac{\sqrt{k}}{\beta^*\omega d}; \frac{500\nu}{d^2\omega}\right) \tag{2.54}$$

In the above equations d is the distance from the cell center to the viscous wall boundary and $CD_{k\omega}$ is the positive portion of the cross-diffusion term of Eq.(2.49). The constants of the first set (ϕ_1) are:

$$\gamma_1 = \frac{\beta_1}{\beta^*} - \frac{\sigma_{\omega 1}\kappa^2}{\sqrt{\beta^*}}, \quad \sigma_{k1} = 0.85, \quad \sigma_{\omega 1} = 0.5, \tag{2.55}$$

$$\beta_1 = 0.075, \quad \beta^* = 0.09, \quad \kappa = 0.41, \quad \alpha_1 = 0.31 \tag{2.56}$$

$$\gamma_2 = \frac{\beta_2}{\beta^*} - \frac{\sigma_{\omega 2}\kappa^2}{\sqrt{\beta^*}}, \quad \sigma_{k2} = 1.0, \quad \sigma_{\omega 2} = 0.856, \quad \beta_2 = 0.0828 \tag{2.57}$$

Menter also provides us in [55] a limit for the production term:

$$\tau_{ij}\frac{\partial u_i}{\partial x_j} = \min(\tau_{ij}\frac{\partial u_i}{\partial x_j}, 20\beta^*\rho K\omega) \tag{2.58}$$

Boundary Conditions

The boundary conditions are referred to [53]:

$$\frac{U_\infty}{L} < \omega_\infty < 10\frac{U_\infty}{L}, \quad \frac{10^{-5}U_\infty^2}{Re_L} < k_\infty < \frac{10^{-1}U_\infty^2}{Re_L} \tag{2.59}$$

$$\omega_{\text{wall}} = \frac{6\nu}{\beta_1 d_1^2}, \quad k_{\text{wall}} = 0 \tag{2.60}$$

where L is the approximate length of the computational domain and d_1 is the distance to the next point off the wall.

This page is intentionally left blank.

Chapter 3

Results

3.1 Problem formulation

Figure 3.1 presents the computational domain of the flow configuration. A two-dimensional NACA0012 foil with a chord length of $L = 1m$ is positioned in a uniform flow with velocity $U = 1m/s$ along the x-axis. The foil's leading edge is situated at the origin of the Cartesian coordinate system. The movement of the foil's midline is described by the following travelling wave equation.

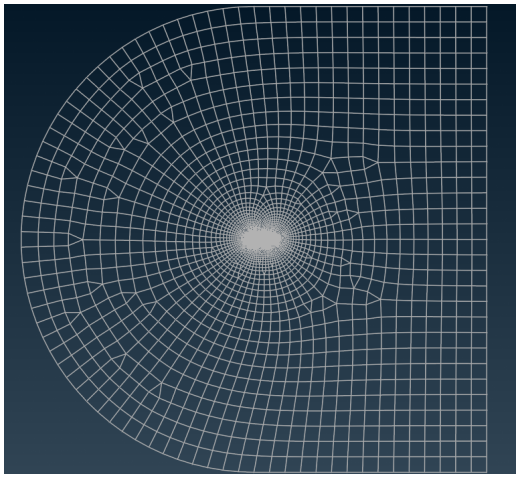

Figure 3.1: Computational mesh.

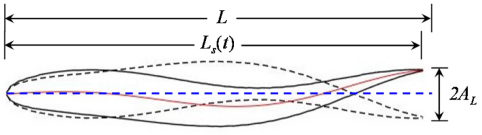

Figure 3.2: Foil's parameters.

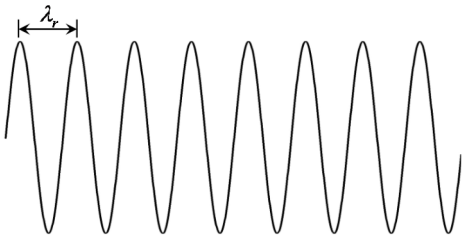

Figure 3.3: Travelling wavy motion.

$$y(x,t) = A(x)\sin\left[2\pi\left(\frac{x}{\lambda_r} - \frac{t}{T}\right)\right] \tag{3.1}$$

where $A(x)$ is the amplitude of the foil's midline oscillation defined as a second degree polynomial $A(x) = a_0 + a_1 x + a_2 x^2$ with $a_0 = 0$, $a_1 = 0.05$ and $a_2 = 0$ [56], x is calculated from the leading edge, y is the transverse displacement, λ_r is the

real wavelength as shown in figure 3.2 and T is the period of the oscillation. The following constraint for the midline's length must always hold true:

$$\int_0^{L_s(t)} \sqrt{1 + \left(\frac{\partial y}{\partial x}\right)^2}\, dx = L \tag{3.2}$$

where $L_s(t)$ is the foil's projected length to the x-axis. The outline of the undulation is shown in figure 3.3, where it is clear that $L_s(t)$ is a variable dependent on time. This constraint is mandatory because in reality fish cannot stretch or shrink in order to change their midline length. Thus, $L_s(t) < L$ must always hold true while swimming.

Reynolds and Strouhal numbers are known as:

$$St = \frac{2A(L)}{UT} \tag{3.3}$$

$$Re = \frac{UL}{\nu} \tag{3.4}$$

where $A(L) = 0.05$ and ν is the kinematic viscosity of the fluid.

The time-mean thrust coefficient $\overline{C}_T$ is defined as:

$$\overline{C}_T = \frac{1}{T}\int_t^{t+T} C_T\, dt = \frac{1}{T}\int_t^{t+T} \frac{-F_x(t)}{0.5\rho U^2 L}\, dt \tag{3.5}$$

where C_T is the instantaneous thrust coefficient, $F_x(t)$ is the drag force acting in the x-axis and ρ is the density of the fluid. Therefore, if $\overline{C}_T < 0$ the foil feels a time-mean drag force and respectively if $\overline{C}_T > 0$ it feels a time-mean thrust force.

The computational domain is a combination of a semicircle with radius that of $60 \times L$ and a rectangular with dimensions of $60L \times 120L$ (see figure 3.1). The inlet velocity boundary is located at a distance of $60L$ from the leading edge of the foil, where $\mathbf{u} = (U, 0)$ and $\frac{\partial p}{\partial x} = 0$. The outflow boundary is $59L$ downstream, with $\frac{\partial \mathbf{u}}{\partial x} = (0, 0)$ and $\frac{\partial p}{\partial x} = 0$ (no-stress outflow boundary conditions).

The flow domain is divided into three grid zones: 1, 2, and 3 (figure **??**). The first zone features a regular grid with medium resolution. The second zone si a rectangular area around the foil with dimensions $10.2L \times 7.2L$ with high resolution. And finally, the third zone represents the boundary layer and utilizes a very high resolution grid. Unstructured meshes are used in the first and second zones and structured in the third zone.

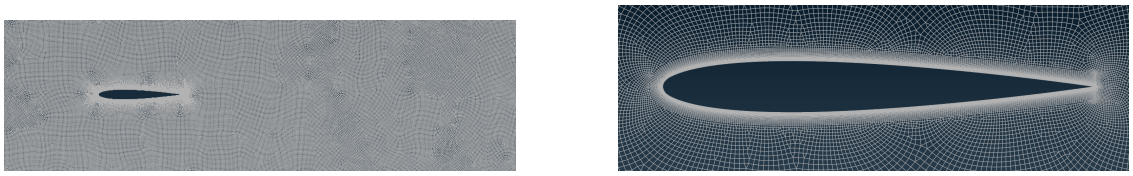

(a) Closer view of mesh around the foil. (b) Boundary layer of the foil.

Figure 3.4: Zoomed-in views of the computational grid.

3.2 Grid Independence

The mesh independence test was conducted at $(St, Re, \lambda) = (0.6, 50000, 1.0)$. At a time step of $\Delta t = 1.5432 \times 10^{-4} T$ the grid-independence test was performed for grid numbers 8.9×10^4 (N_1), 1.1×10^5 (N_2), and 3.4×10^5 (N_3), which correspond to 152, 317, and 704 points on the surface of the foil, respectively. Figure 3.5 illustrates the thrust coefficient over two periods of oscillation and we find out that there is no significant difference between N_2 and N_3, so the N_2 is adopted for all calculation due to its efficient computational cost.

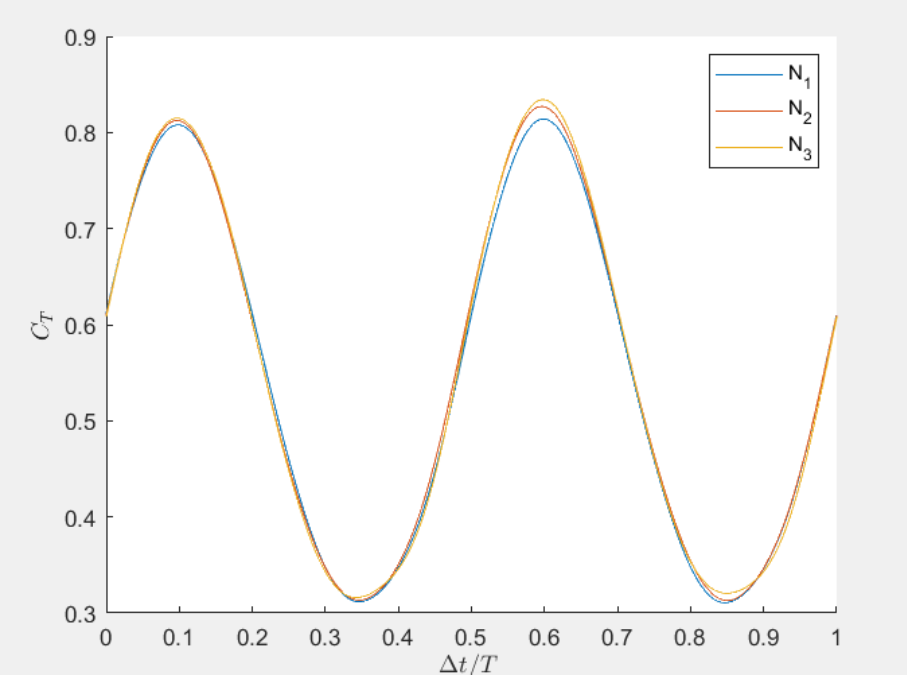

Figure 3.5: Mesh independence test at $(St, Re, \lambda) = (0.6, 50000, 1.0)$. N_2 is adopted due to its insignificant difference from N_3 and its efficiency.

3.3 Temporal Independence

The time independence test was conducted at $(St, Re, \lambda) = (0.6, 50000, 1.0)$. At a mesh with grid number 1.1×10^5 the time independence test was performed with time steps of $1.8519 \times 10^{-4}T$ (Δt_1), $1.5432 \times 10^{-4}T$ (Δt_2), and $9.26 \times 10^{-5}T$ (Δt_3). The computed results, shown in figure 3.6, indicate that Δt_2 is sufficient enough to ensure both accuracy and computational efficiency.

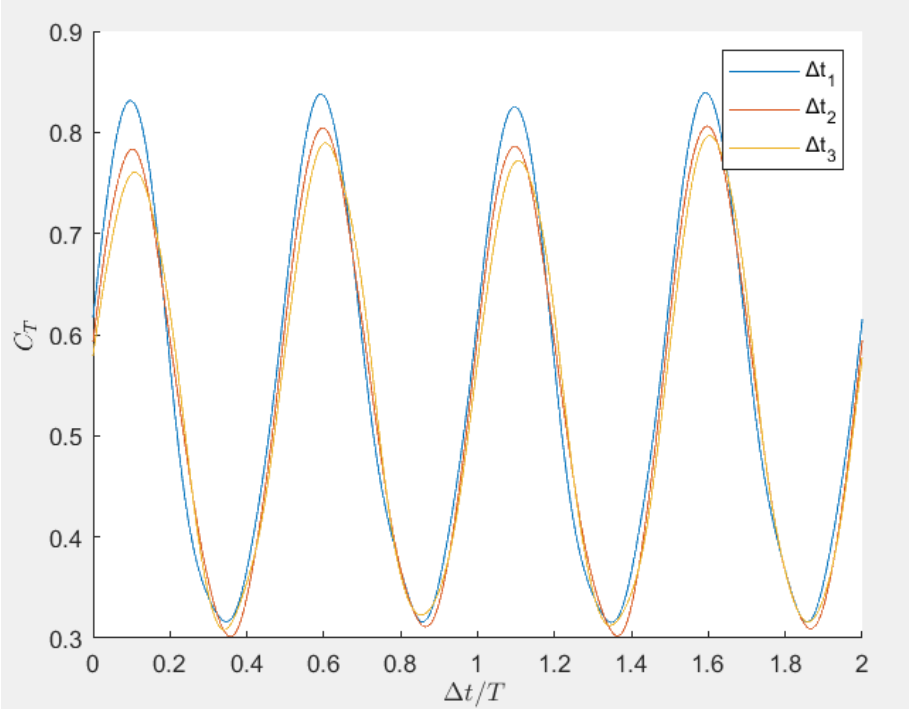

Figure 3.6: Time independence test at $(St, Re, \lambda) = (0.6, 50000, 1.0)$. Δ_2 is adopted due to its insignificant difference from Δ_3 and its efficiency.

3.4 Thrust dependence on Re, St and λ

To examine the thrust produced by the travelling wavy foil, we conducted a systematic study of the time-averaged thrust force on the foil. The study covered a range of Strouhal numbers, $St = (0.2, 0.4, 0.6, 0.8, 1.0)$, Reynolds numbers, $Re = (10000, 25000, 50000, 100000, 200000)$ and wavelengths, $\lambda = (0.5, 0.67, 1.0, 1.5, 2.0)$. The findings on thrust generation are discussed first, followed by the comparison of thrust coefficient in laminar and turbulent flows and the contours of vorticity and pressure.

Figures 3.7(a)-(e) demonstrate how $\overline{C}_T$ depends on St, and λ for different values of Reynold's number. As one can see, $\overline{C}_T$ is linearly proportional to that of $St^3\lambda$. The dotted line is the function $y = x$. Interesting is the fact that at low Re and St numbers the thrust coefficient is negative which means that the foil is experiencing drag $\left(\overline{C}_T < 0\right)$. Increasing Re and St we found that thrust is increased but is more

sensitive to St rather than Re which indicates that viscosity and inertia both play a crucial role in thrust while inertia is the most effective factor of the two, as shown in 3.15 and 3.16. Keeping St and Re constant and changing λ we find that the relation between thrust and λ is linear. It's obvious that a small λ blocks the flow around the foil's surface thus generating less thrust. While St and λ are kept the same $\overline{C}_T$ increases as Re increases, which means that its easier to accelerate at higher speeds. This phenomenon can be explained as the viscous effect is more weakened and the added mass is decreased in higher speeds.

The linear least-squares regression is applied to determine the relationship between $\overline{C}_T$, St, and λ, resulting in the expression $\overline{C}_T = c_1 St^3 \lambda + c_2$, with five examples illustrated in figure 3.7. The coefficients are found to be

$$c_1 = (1.738, 1.793, 1.820, 1.833, 1.844)$$

and $c_2 = (0.087, 0.105, 0.115, 0.119)$ for $Re = (10000, 25000, 50000, 100000, 200000)$, respectively, as shown in figures 3.8a and 3.8b.

The dependence of c_1 and c_2 on Re (for all values of Re examined) can be expressed as $c_1 = 1.467 Re^{0.0193}$ and $c_2 = 0.0354 Re^{0.1036}$. Hence, the unified relationship between $\overline{C}_T$, St, Re, and λ is given by:

$$\overline{C}_T = 1.467 Re^{0.0193} St^3 \lambda + 0.0354 Re^{0.1036} \tag{3.6}$$

Equation 3.6 shows how the three parameters, St, Re and λ, have an impact on the thrust generation of the foil. Particularly, $overline C_T$ increases at a slow pace while increasing Re ,as mentioned before, and the exact opposite with higher numbers of λ and especially with St. If we look closely to the second term of the right hand side we find that this term participates more in percentage terms as Re is getting higher. Figure 3.9 demonstrates C_T during one oscillation period at five different combinations of St and Re for every λ. Figures 3.10 - 3.14 display dimensionless spanwise vorticity structures for five selected cases. Figures 3.15 and 3.16 present how Re and St affect $\overline{C}_T$ respectively while keeping one constant and changing the other.

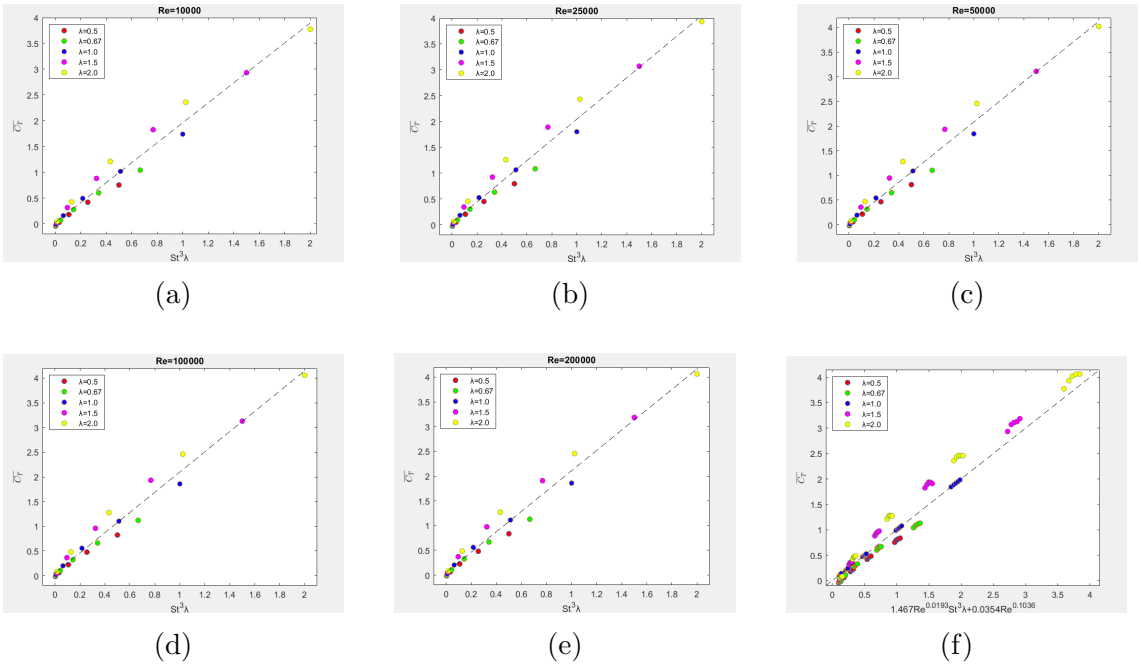

(a) (b) (c)

(d) (e) (f)

Figure 3.7: (a-e) Time-mean thrust coefficient $\overline{C}_T$ as a function of Strouhal number St and wave length λ, denoted as $\overline{C}_T = c_1 St^3\lambda + c_2$. The dash line is the linear least-squares regression line. (f) Relationship of $\overline{C}_T$ with St, Re and λ for the travelling wavy foil. The dash line denotes a linear function with coefficient equal to one.

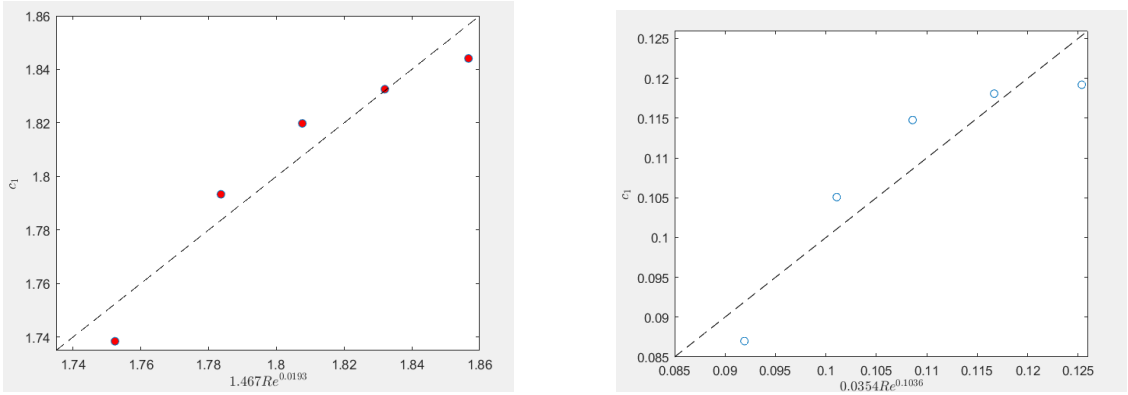

(a) (b)

Figure 3.8: (a),(b) Dependence of c_1 and c_2 on Re. The dash lines denote a linear function with coefficient equal to one.

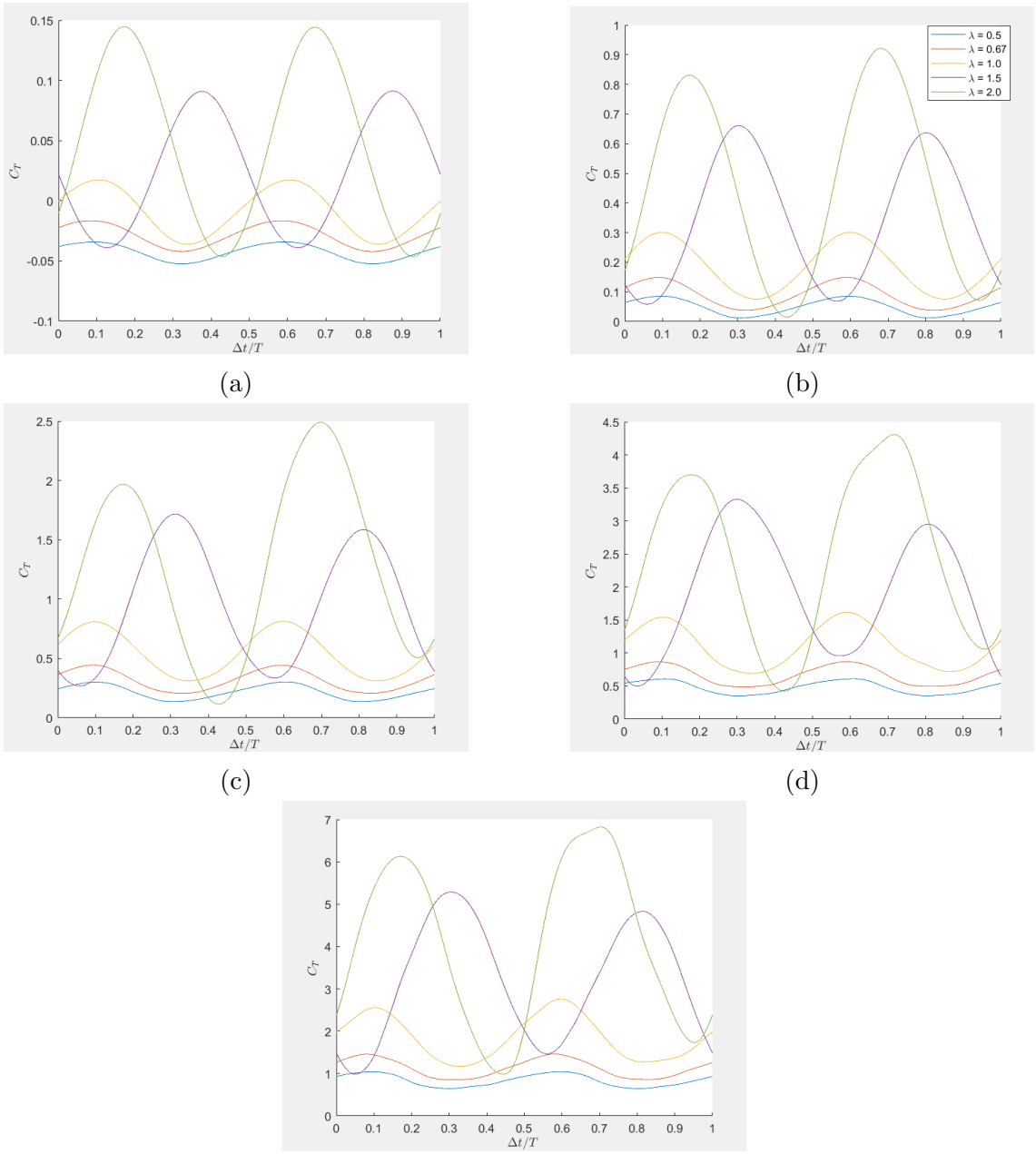

(a) (b) (c) (d) (e)

Figure 3.9: (a)-(e) Thrust coefficient oscillation during one period for $(St, Re) = [(0.2, 10000), (0.4, 25000), (0.6, 50000), (0.8, 100000), (1.0, 200000)]$ respectively. It's obvious that by increasing St and Re, $\overline{C}_T$ is also increased. Increasing λ, $\overline{C}_T$ oscillation amplitude is larger.

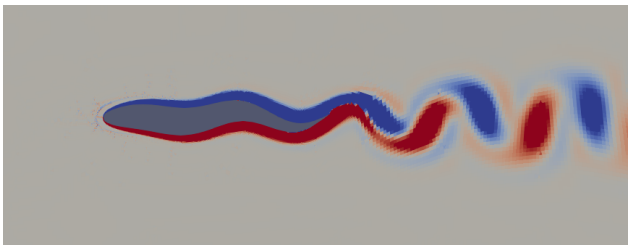

(a)

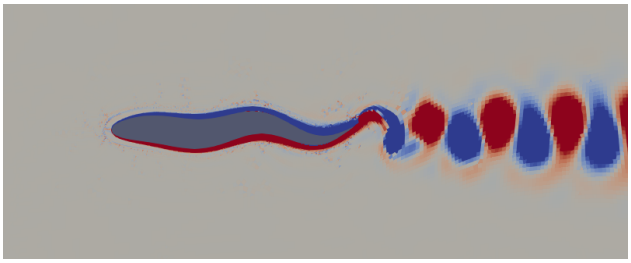

(b)

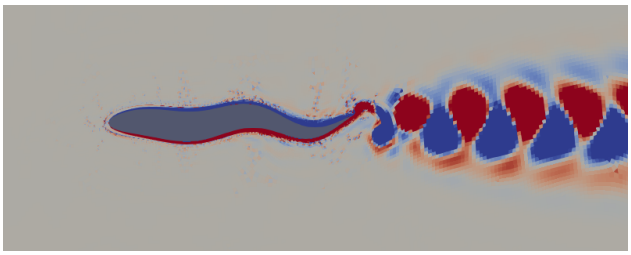

(c)

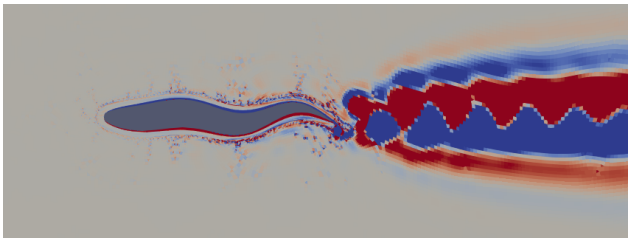

(d)

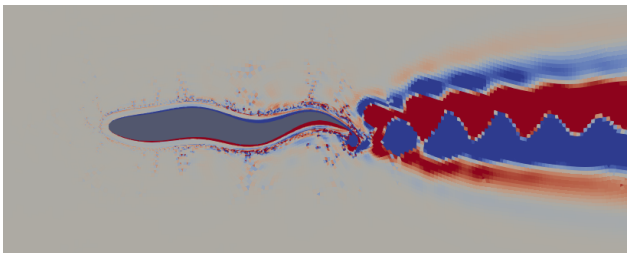

(e)

Figure 3.10: Contours of spanwise vorticity for $\lambda = 0.5$. The red and blue colors denote positive and negative vorticity respectively. (a) $(St, Re) = (0.2, 10000)$, (b) $(St, Re) = (0.4, 25000)$, (c) $(St, Re) = (0.6, 50000)$, (d) $(St, Re) = (0.8, 100000)$, (e) $(St, Re) = (1.0, 200000)$

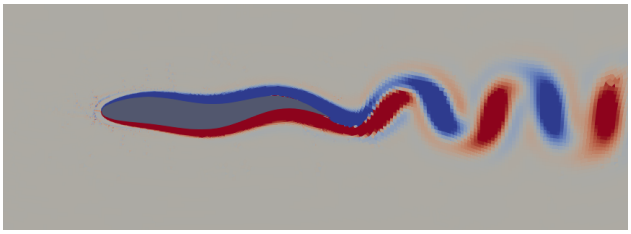

(a)

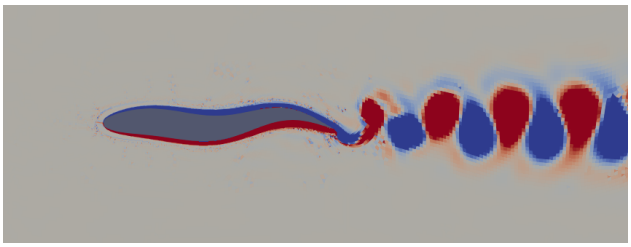

(b)

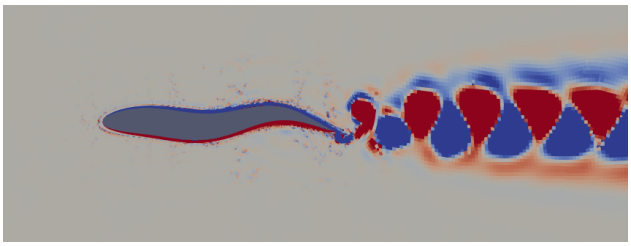

(c)

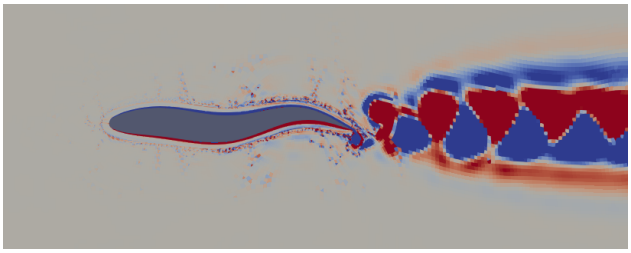

(d)

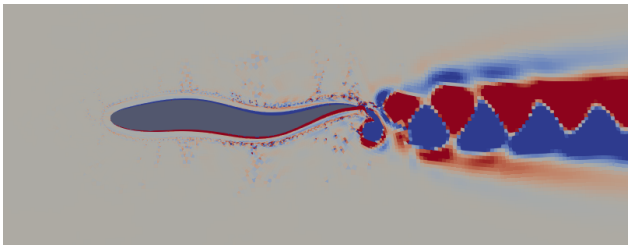

(e)

Figure 3.11: Contours of spanwise vorticity for $\lambda = 0.67$. (a) $(St, Re) = (0.2, 10000)$, (b) $(St, Re) = (0.4, 25000)$, (c) $(St, Re) = (0.6, 50000)$, (d) $(St, Re) = (0.8, 100000)$, (e) $(St, Re) = (1.0, 200000)$

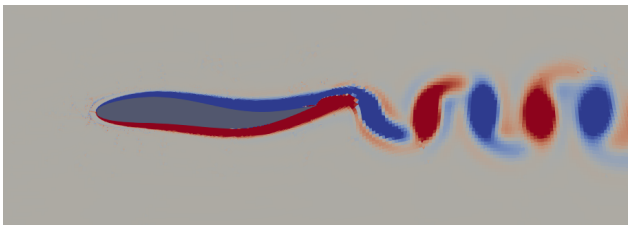

(a)

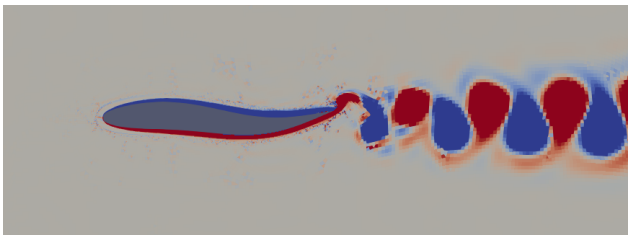

(b)

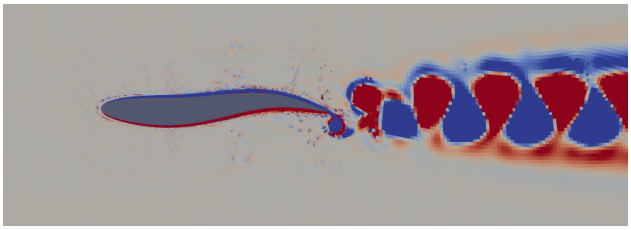

(c)

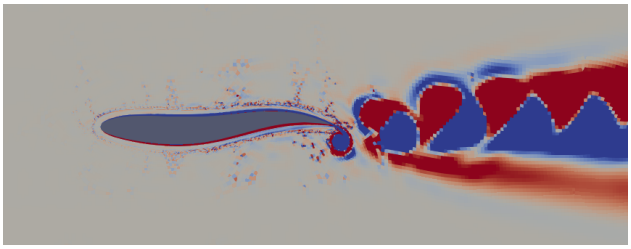

(d)

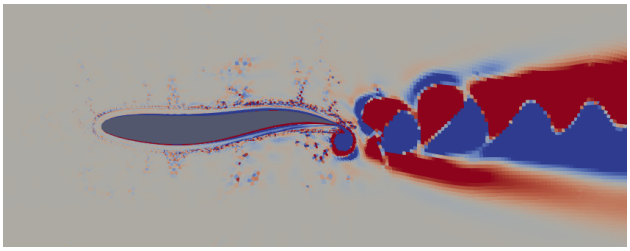

(e)

Figure 3.12: Contours of spanwise vorticity for $\lambda = 1.0$. (a) $(St, Re) = (0.2, 10000)$, (b) $(St, Re) = (0.4, 25000)$, (c) $(St, Re) = (0.6, 50000)$, (d) $(St, Re) = (0.8, 100000)$, (e) $(St, Re) = (1.0, 200000)$

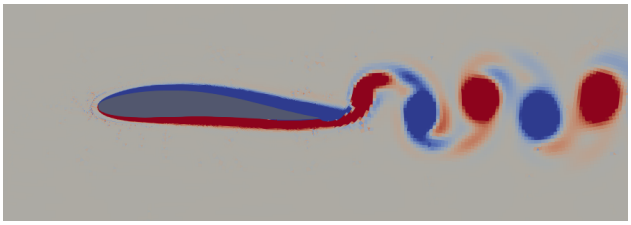

(a)

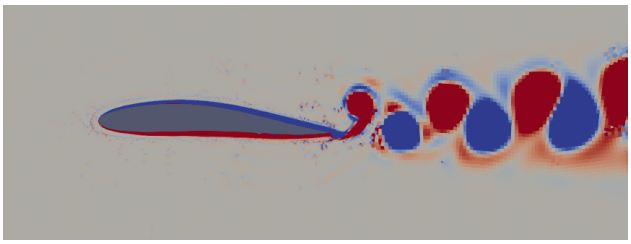

(b)

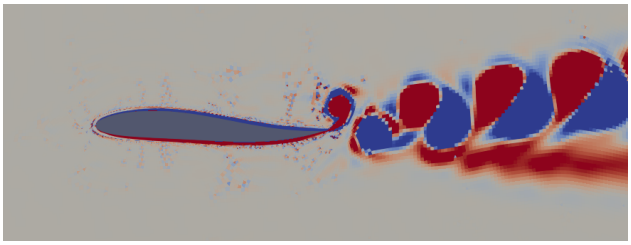

(c)

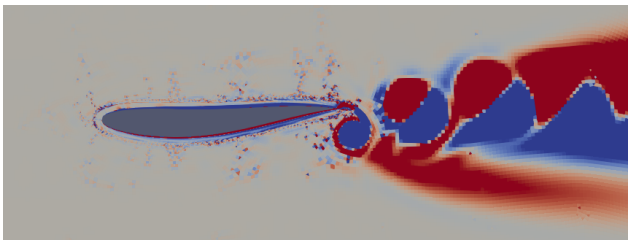

(d)

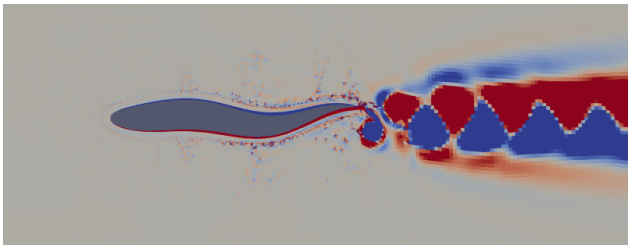

(e)

Figure 3.13: Contours of spanwise vorticity for $\lambda = 1.5$. (a) $(St, Re) = (0.2, 10000)$, (b) $(St, Re) = (0.4, 25000)$, (c) $(St, Re) = (0.6, 50000)$, (d) $(St, Re) = (0.8, 100000)$, (e) $(St, Re) = (1.0, 200000)$

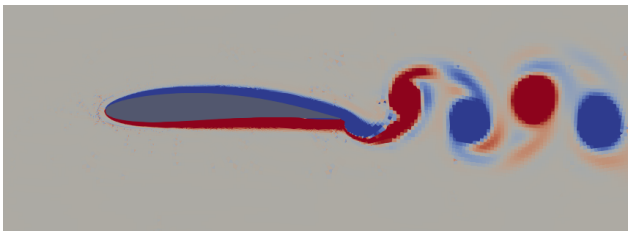

(a)

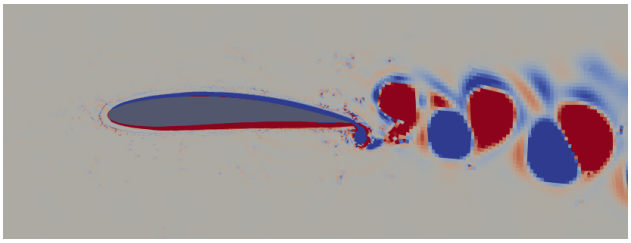

(b)

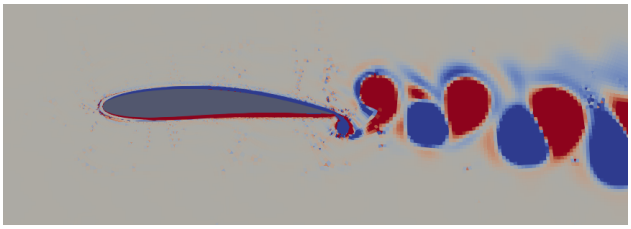

(c)

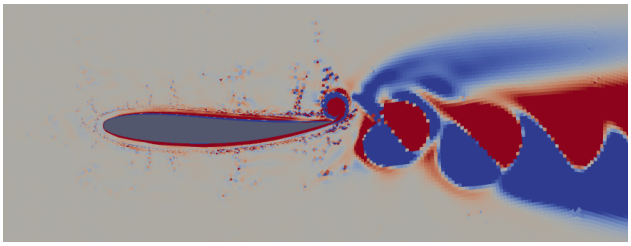

(d)

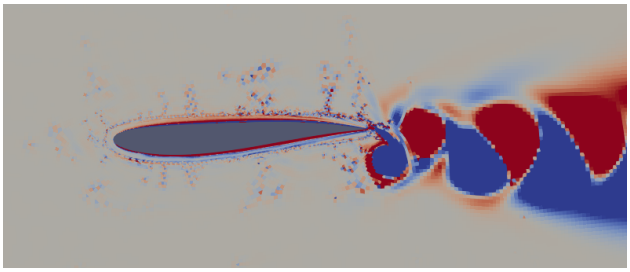

(e)

Figure 3.14: Contours of spanwise vorticity for $\lambda = 2.0$. (a) $(St, Re) = (0.2, 10000)$, (b) $(St, Re) = (0.4, 25000)$, (c) $(St, Re) = (0.6, 50000)$, (d) $(St, Re) = (0.8, 100000)$, (e) $(St, Re) = (1.0, 200000)$

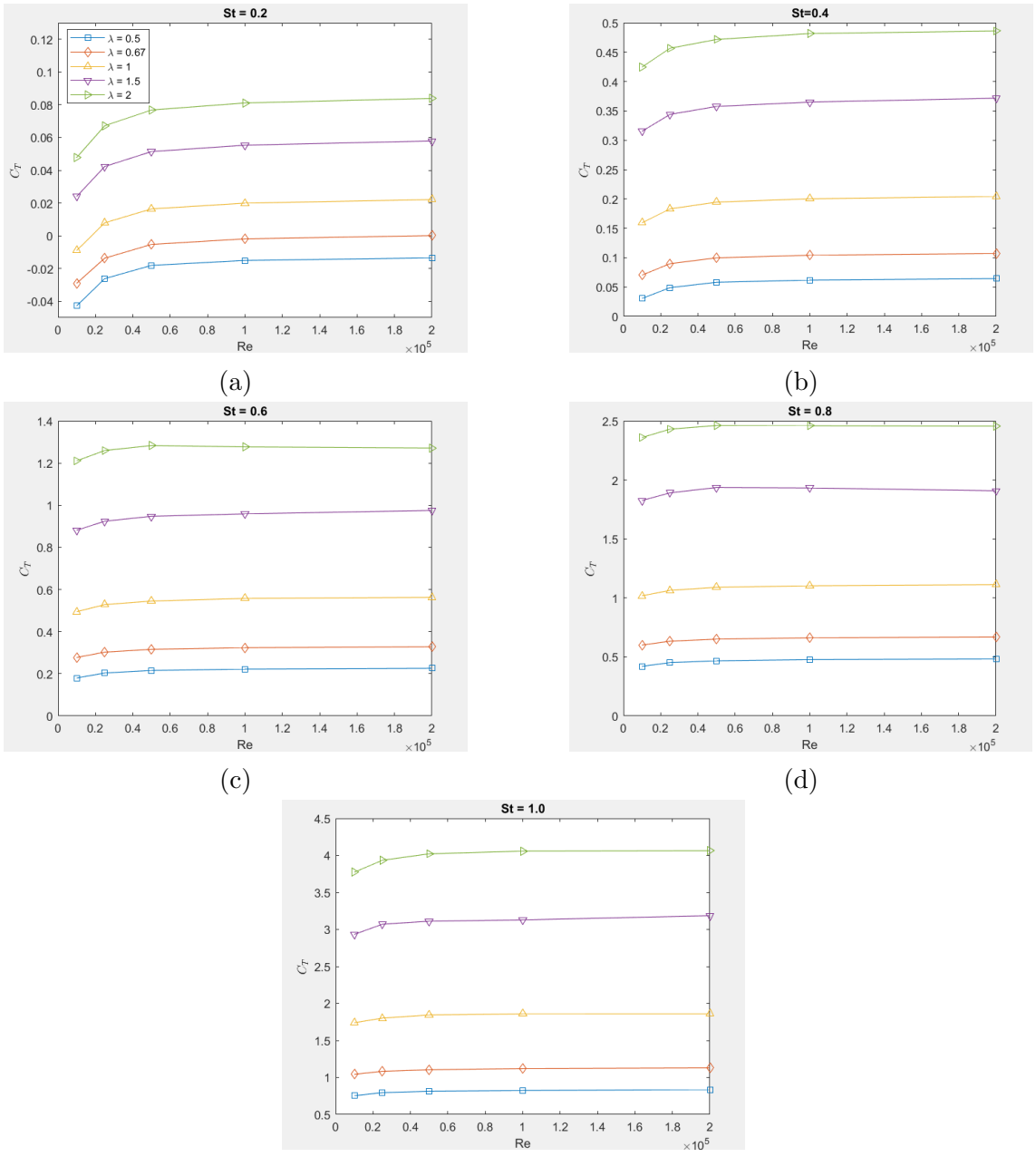

Figure 3.15: Effect of Re on $\overline{C}_T$. Increasing St and λ we get higher values of $\overline{C}_T$. Re doesn't contribute as much as St and λ

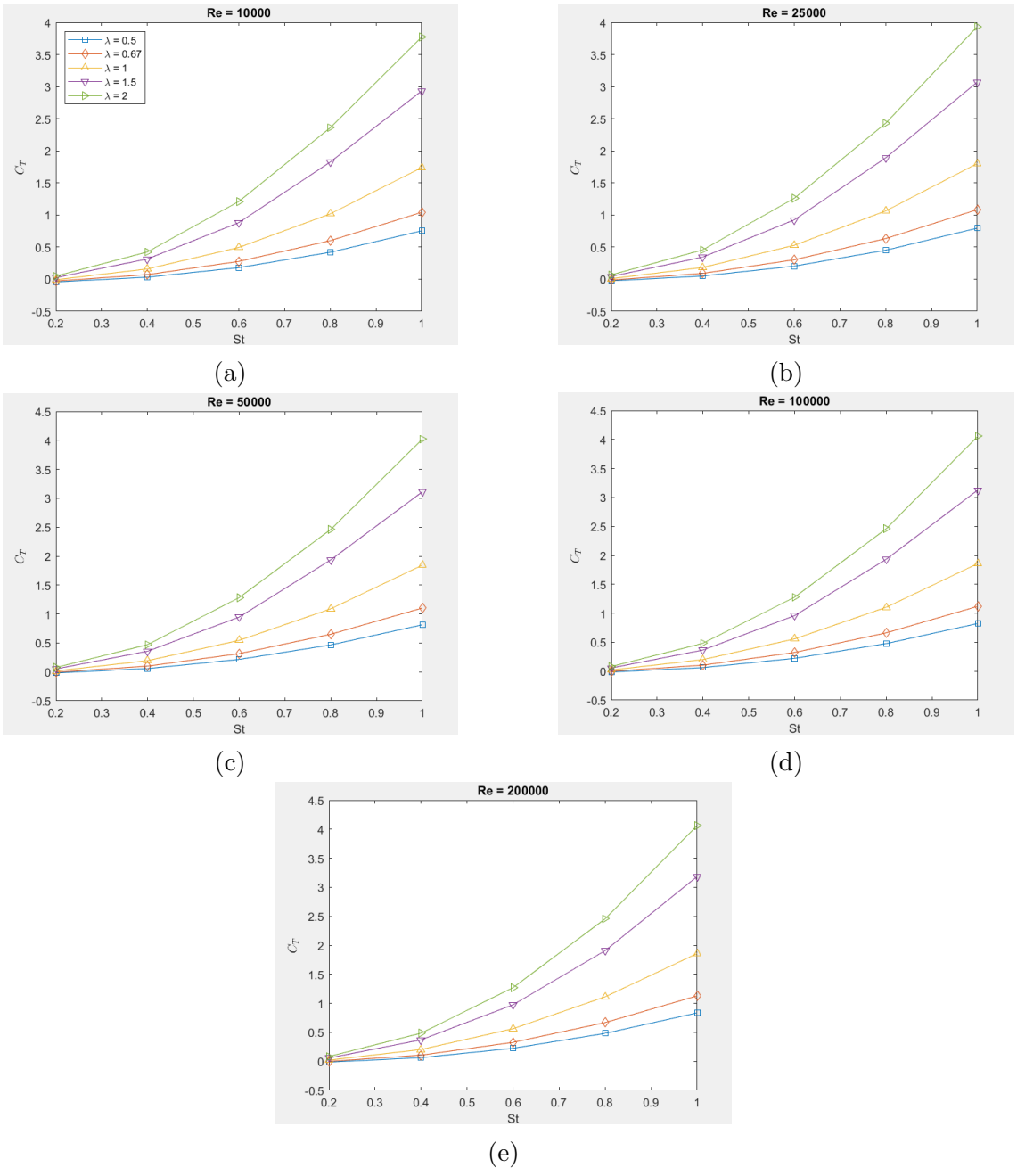

Figure 3.16: Effect of St on $\overline{C}_T$. There is an exponential growth of $\overline{C}_T$ when increasing St and λ at the same time. It's observed that with higher values of Re, $\overline{C}_T$ is minimally affected.

3.5 Comparison between Laminar and Turbulent Flow

Comparing the results from this study and the one of Li-Ming Chao et al. [57] which performed similar calculations for smaller values of Re we find that slender swimmers experience difference C_T in laminar and turbulent flow.

At first glance, in laminar flow $\overline{C}_T$ has smaller values than those in turbulent flow with is logical because, as mentioned before, $\overline{C}_T$ increases in higher Re. We can also observe from figure 3.17 that going from laminar to turbulent the relation of $\overline{C}_T$ with $St^3\lambda$ keeps linear.

Figure 3.18a illustrates that c_1 and c_2 are more sensitive to Re and thus $\overline{C}_T$ is too, as shown in figure 3.18b. Thus, going from laminar to turbulent flow $\overline{C}_T$ becomes less sensitive to Re and more reliant to St and λ. This means that a small fish, being the prey, is getting an advantageous C_T at smaller Re and a big fish, being the predator, gets higher C_T by increasing St at high Re.

Comparing figures 3.19 and 3.9 one can observe that in both cases of laminar and turbulent flows the thrust coefficient performs almost identical oscillations with the only difference that in laminar flow there are cases that C_T is negative which means that the foil is experiencing drag. Also, the amplitudes are bigger in turbulent flow which is expected due to higher values of Re.

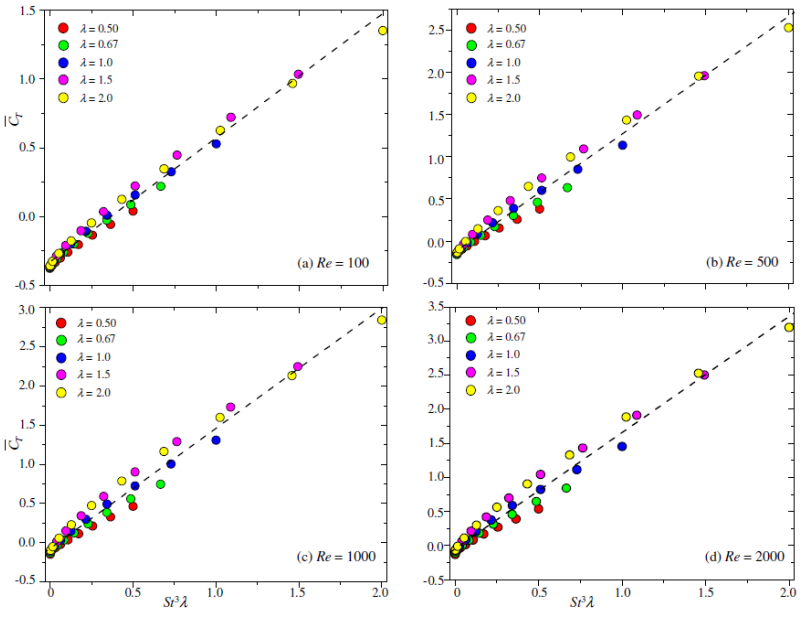

Figure 3.17: Time-mean thrust coefficient $\overline{C}_T$ as a function of Strouhal number St and wave length λ, denoted as $\overline{C}_T = St^3\lambda$ for small Re, from [57].

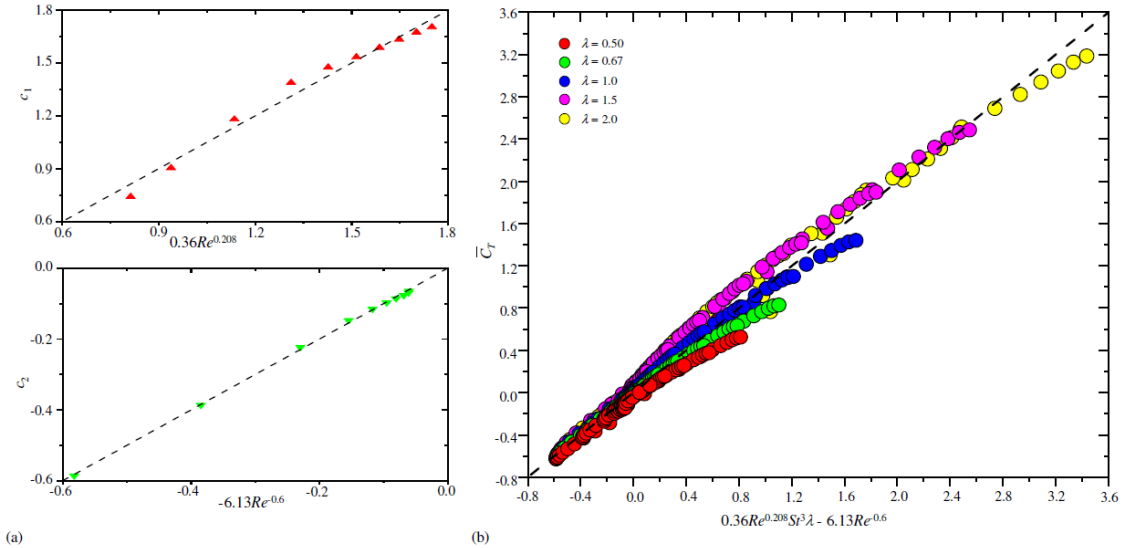

Figure 3.18: (a) Dependence of c_1 and c_2 on Re. (b) Relationship of $\overline{C}_T$ with St, Re and λ for the travelling wavy foil for small Re, from [57].

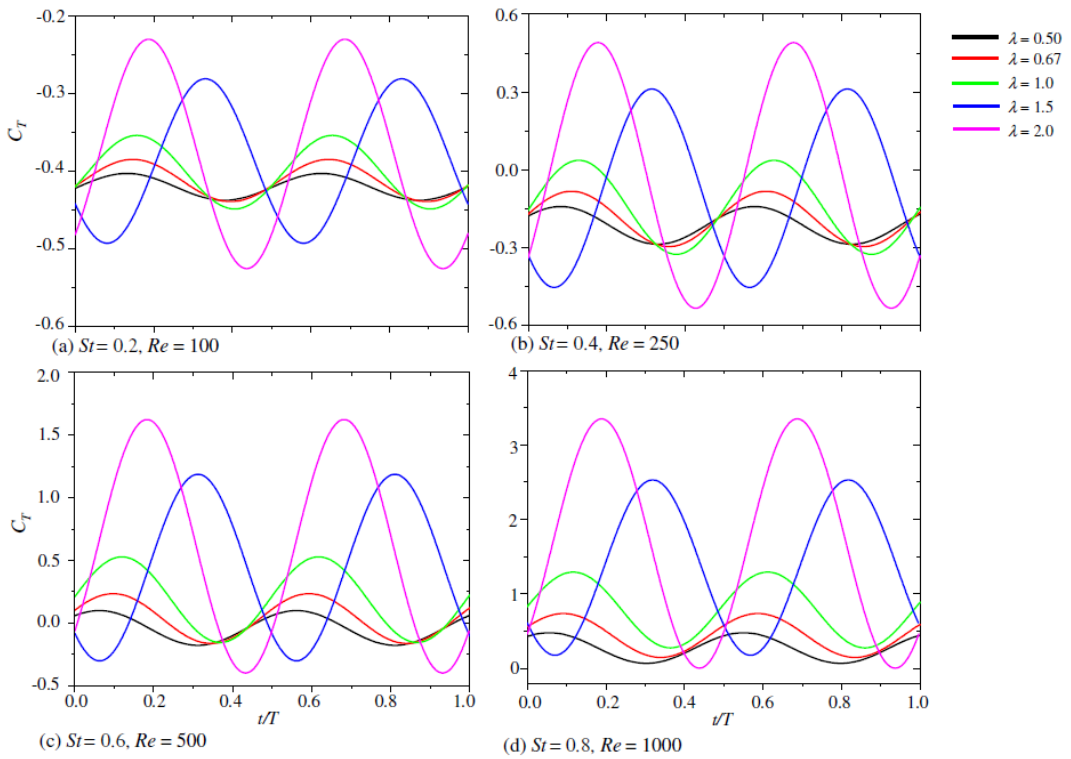

Figure 3.19: Thrust coefficient oscillation during one period for low Reynolds, from [57].

This page is intentionally left blank.

Chapter 4

Conclusions

4.1 Summary

A numerical analysis was conducted using an Eulerian solver, MaPFlow, to evaluate the hydrodynamic performance of a fish-like foil performing a travelling wave undulation. The calculations were performed considering $St = 0.2 - 1.0$ with $\Delta St = 0.2$, $Re = (10000, 25000, 50000, 100000, 200000)$, and a non-dimensional wavelength $\lambda = (0.5,$
$0.67, 1.0, 1.5, 2.0)$. The foil length was kept constant to simulate the swimming behaviour of a typical slender swimmer. When the foil length is fixed at L, the projected streamwise length L_s of the undulating foil becomes time-dependent, with $L_s(t) \leq L$ over one oscillation cycle. The average value of $L_s(t)$ increases as λ gets larger.

The study focuses on how St, Re, and λ affect thrust generation. The mean thrust coefficient $\overline{C}_T$ is plotted on the $St^3\lambda - Re$ plane for various values of λ. A relationship between $\overline{C}_T$, St, Re, and λ is found, expressed as $\overline{C}_T = 1.467Re^{0.0193}St^3\lambda + 0.0354Re^{0.1036}$. This shows that $\overline{C}_T$ increases with higher values of St, Re, and λ. However, the increase of $\overline{C}_T$ due to the increase of Re is relatively low compared to the other two parameters.

Finally, a comparison is made between $\overline{C}_T$ and C_T in laminar and turbulent flow. It is found that C_T oscillations have similar form in both flows but with larger amplitudes in the later. As far as $\overline{C}_T$ is concerned, it is also found that in turbulent flow, where Re is large, the coefficient reaches higher values than those in laminar flow and also mostly positive values where in the case of low Re, $\overline{C}_T$ is negative and the foil is experiencing drag ($\overline{C}_T < 0$).

4.2 Future Work

While this thesis has provided valuable insights into biomimetics and especially the efficiency of a foil mimicking fish's motion several areas require deeper analysis.

First, the current research was limited to study only a small portion of parameters, while using approximate formulas to calculate the results needed, due to time and computational power availability, and expanding the scope to include more

values for the chosen parameters could offer a more comprehensive understanding. Additionally, using the exact formulas for calculating the drag or thrust coefficients and increasing mesh density should decrease the error of all calculations providing more accurate results. Furthermore, future studies should consider continuing this research by applying fluid-structure interactions using the Finite Element Method (FEM) to examine deformations of the foil due to pressure. It's important to mention that revising this study in three dimensions while also examining C_P, added mass and efficiency, η, would be challenging. Another interesting idea would be to take into consideration the angle of attack and examine the way it's affecting the fish motion in general and especially C_T and η by changing this parameter. Finally, a study could investigate how a hydrophobic material for the foil reduces its drag and affects the wake form.

Finally, as technological advancements continue to emerge, exploiting newer tools and techniques could enhance data accuracy and analytical precision by experimenting with live models and ultimately leading to deeper and more precise conclusions.

Bibliography

[1] Swagat Chutia, Nayan M. Kakoty, and Dhanapati Deka. "A Review of Underwater Robotics, Navigation, Sensing Techniques and Applications". In: *AIR '17: Proceedings of the 2017 3rd International Conference on Advances in Robot* (2017).

[2] Jian Wang et al. "Development and Control of Underwater Gliding Robots: A Review". In: *IEEE* (2022).

[3] Maria L. Castaño and Xiaobo Tan. "Model Predictive Control-Based Path-Following for Tail-Actuated Robotic Fish". In: *Dynamic Systems, Measurement and Control* (2019).

[4] Michael S. Triantafyllou and George S. Triantafyllou. "An Efficient Swimming Machine". In: *Scientific American* (1995).

[5] J. Gray. *Animal Locomotion*. 1968.

[6] J. Bell Pettigrew. *Animal locomotion, or, walking, swimming, and flying, with a dissertation on aeronautics*. 1874.

[7] C. M. Breder. "The locomotion of fishes". In: *Zoologica* (1926).

[8] J. Gray. "Studies in animal locomotion. VI. The propulsive powers of the dolphin." In: *The Journal of Experimental Biology* (1936).

[9] Taylor G. "Analysis of the swimming of long and narrow animals." In: *Proceedings of the Royal Society Series A* (1952).

[10] M. J. Lighthill. "Note on the swimming of slender fish." In: *Journal of Fluid Mechanics* (1960).

[11] Webb P. W. "Hydrodynamics and energetics of fish propulsion." In: *Fisheries Research Board of Canada* (1975).

[12] Lindsey C.C. "Form, function and locomotory habits in fish". In: *Fish Physiology* (1978).

[13] Davies J.B.C. Sfakiotakis M. Lane D.M. "Review of fish swimming modes for aquatic locomotion". In: *IEEE Journal of Oceanic Engineering* (1999), pp. 237–252.

[14] B. Wu et al. "The Effects of Caudal Fin's Bending Stiffness on a Self-Propelled Carangiform Swimmer." In: *Physics of Fluids* (2022).

[15] J.A. Cole, G. Loubimov, and Kinzel M. "Comparison of Computational Methods for Hydrodynamic Performance Prediction of Oscillating Marine Propulsors." In: *Ocean Engineering* (2021).

[16] C. Wei et al. "Performance evaluation and optimization for two-dimensional fish-like propulsion". In: *Ocean Engineering* (2021).

[17] Martin A.K., Anathakrishanan P., and Krishnankutty P. "Ship hull wake effect on the hydrodynamic performance of a heave–pitch combined oscillating fin". In: *Ships and Offshore Structures* (2021).

[18] Alberti L. et al. "A Computational Fluid Dynamics Investigation of a Flapping Hydrofoil as a Thruster". In: *Biomimetics* (2023).

[19] Parameswaran Krishnankutty Harikrishnan Vijayakumaran. "Computational Fluid Dynamics Study of a Flexible Flapping Hydrofoil Propulsor". In: *American Society of Mechanical Engineers* (2016).

[20] Ravi Chaithanya Mysa and Pablo Valdivia y Alvarado. "The effect of batoid inspired undulating motions on the propulsive forces of a circular planform." In: *Physics of Fluids* (2021).

[21] Mitra S. et al. "Design and Control Strategy of Bio-Inspired Underwater Vehicle with Flexible Propulsor." In: *Journal of Modern Mechanical Engineering and Technology* (2021).

[22] Qiao-Gao Huang et al. "Numerical investigations on the thrust generation of a manta-inspired foil". In: *Modern Physics Letters B* (2020).

[23] Qiao-gao Huang, Dong Zhang, and Guang Pan. "Computational Model Construction and Analysis of the Hydrodynamics of a Rhinoptera Javanica". In: *IEEE* (2020).

[24] Haocai Huang et al. "Hydrodynamic analysis and motion simulation of fin and propeller driven manta ray robot". In: *Applied Ocean Research* (2021).

[25] Rakesh Rayapureddi and Santanu Mitra. "Novel Hydrodynamic Analysis Towards Capabilities Improvement of Bio-inspired Underwater Vehicles Using Momentum Redistribution Method". In: *Journal of Bionic Engineering* (2022).

[26] Luo Y. et al. "A Numerical Investigation on Thrust and Torque Production of a Batoid Fish with Asymmetric Pectoral Fins Flapping." In: *Ocean Engineering* (2022).

[27] Isogai K. "Effect of Flexibility of the Caudal Fin on the Propulsive Performance of Dolphins." In: *Transactions of the Japan Society for Aeronautical and Space Sciences* (2014).

[28] Kang Li et al. "Hydrodynamic Analysis of a Gliding Robotic Dolphin Based on Computational Fluid Dynamics." In: *IEEE* (2016).

[29] Xue Z., Li L., and Y. Song. "The Research of Maneuverability Modeling and Environmental Monitoring Based on a Robotic Dolphin." In: *Applied Bionics and Biomechanics* (2021).

[30] Cao J. et al. “Numerical Exploration on Pitching Motion of Robotic Dolphin Realized by Pectoral Fin.” In: *IEEE* (2021).

[31] Pan Han et al. “Kinematics and Hydrodynamics of a Dolphin in Forward Swimming.” In: *AIAA AVIATION Forum* (2020).

[32] Dan Xia et al. “A Comparative and Collaborative Study of the Hydrodynamics of Two Swimming Modes Applicable to Dolphins.” In: *Biomimetics* (2023).

[33] Feng D. et al. “Numerical Study on Hydrodynamic Behavior of Flexible Multi-Stage Propulsion Foil.” In: *AIP Advances* (2021).

[34] D. W. Bechert, M. Bruse, and W. Hage. “W. Experiments with Three-Dimensional Riblets as an Idealized Model of Shark Skin.” In: *Experiments in Fluids* (2000).

[35] Min Liu and Liran Ma. “Drag Reduction Methods at Solid-Liquid Interfaces.” In: *Friction* (2022).

[36] Mahdi Tabatabaei Malazi. “Design optimization of a longfin inshore squid using a genetic algorithm”. In: *Ocean Engineering* (2023).

[37] Xixing He et al. “Bidirectional Underwater Drag Reduction on Bionic Flounder Two-Tier Structural Surfaces”. In: *Biomimetics* (2023).

[38] Jin Shi et al. “Effect of the Biomimetic Spine-Covered Protrusions (BSCPs) Height and Arrangement on SUBOFF Bare Hull Model Drag”. In: *Arabian Journal for Science and Engineering* (2023).

[39] Xiaoming Feng et al. “Coupled Bionic Drag-Reducing Surface Covered by Conical Protrusions and Elastic Layer Inspired from Pufferfish Skin.” In: *ACS Surfaces, Interfaces, and Applications* (2022).

[40] Guizhong Tian et al. “Numerical-Experimental Study on the Influence of the Biomimetic Spine-Covered Protrusions (BSCPs) Structure on the Base Pressure and Near-Wake Flow of Underwater Vehicles”. In: *Arabian Journal for Science and Engineering* (2022).

[41] Ren X. et al. “Design and Analysis of Underwater Drag Reduction Property of Biomimetic Surface with Micro-Nano Composite Structure.” In: *In Advances in Mechanical Design* (2019).

[42] Yunxin Xu et al. “Hydrodynamic Investigation of a Remora-Inspired Autonomous Underwater Vehicle Docking Onto a Benchmark Submarine.” In: *Ocean Engineering* (2024).

[43] D. Chrismianto, AWB Santosa, and A. Wirahutama. “Analysis of Leading Edge Protuberances on Fully Submerged Hydrofoil of 15 m Pilot Boat.” In: *IOP Conference Series: Earth and Environmental Science* (2021).

[44] Tom A. Smith and Jake Rigby. “Underwater radiated noise from marine vessels: A review of noise reduction methods and technology”. In: *Ocean Engineering* (2022).

[45] Callum Stark and Weichao Shi. “Hydroacoustic and hydrodynamic investigation of bio-inspired leading-edge tubercles on marine-ducted thrusters”. In: *Royal Society Open Science* (2021).

[46] Alex Siu Hong Lau and Xun Huang. “The control of aerodynamic sound due to boundary layer pressure gust scattering by trailing edge serrations”. In: *Journal of Sound and Vibration* (2018).

[47] Zhigao Dang, Zhaoyong Mao, and Wenlong Tian. “Reduction of Hydrodynamic Noise of 3D Hydrofoil with Spanwise Microgrooved Surfaces Inspired by Sharkskin.” In: *Journal of Marine Science and Engineering* (2019).

[48] A. J. Chorin. “A Numerical Method for Solving Incompressible Viscous Flow Problems”. In: *Journal of Computational Physics* (1967).

[49] E. Sozer, C. Brehm, and C. C. Kiris. “Gradient calculation methods on arbitrary polyhedral unstructured meshes for cell-centered cfd solvers”. In: *Journal of the Engineering Mechanics Division* (2014).

[50] Robert F. Kunz et al. “A preconditioned Navier–Stokes method for two-phase flows with application to cavitation prediction”. In: *Computers and Fluids* (2000).

[51] A. de Boer, M.S. van der Schoot, and H. Bijl. “Mesh deformation based on radial basis function interpolation.” In: *Computers and Structures* (2007).

[52] Giancarlo Alfonsi. “Reynolds-Averaged Navier–Stokes Equations for Turbulence Modeling”. In: *Applied Mechanics Reviews* (2009).

[53] F. R. Menter. “Two-Equation Eddy-Viscosity Turbulence Models for Engineering Applications”. In: *AIAA* (1994).

[54] D. C. Wilcox. “Reassessment of the Scale-Determining Equation for Advanced Turbulence Models”. In: *AIAA* (1988).

[55] F. R. Menter. “Zonal Two Equation k-omega Turbulence Models for Aerodynamic Flows.” In: *AIAA* (1993).

[56] John J. Videler. *Fish Swimming*. 1993.

[57] Chao Li-Ming, Mahbub Alam, and Cheng Liang. “Hydrodynamic performance of slender swimmer: effect of traveling wavelength”. In: *Journal of Fluid Mechanics* (2021).